Geochronology of granulitized eclogite from the Ama Drime Massif: implications for the tectonic evolution of the South Tibetan Himalaya.

John M. Cottle[*1†], Micah J. Jessup[2‡], Dennis L. Newell[3], Matthew, S.A. Horstwood[4], Stephen R. Noble[4], Randall R. Parrish[4], David J. Waters[1] and Michael P. Searle[1]

1) Department of Earth Sciences, University of Oxford, Oxford OX1 3PR, U.K.

* E mail: John.Cottle@bgs.ac.uk

2) Department of Geosciences, Virginia Tech, Blacksburg, VA 24061, USA

3) Department of Natural and Environmental Sciences, Western State College of Colorado, Gunnison, CO 81231, USA

4) NERC Isotope Geosciences Laboratory, British Geological Survey, Keyworth, NG12 5GG, UK

† Now at: *NERC Isotope Geosciences Laboratory, British Geological Survey, Keyworth, NG12 5GG, UK*

‡ Now at: *Department of Earth and Planetary Sciences, University of Tennessee, Knoxville, 37996, USA*

Abstract

The Ama Drime Massif (ADM) is an elongate north-south trending antiformal feature that extends ~70 kilometers north across the crest of the south Tibetan Himalaya and offsets the position of the South Tibetan Detachment system (STDS). A detailed U(-Th)-Pb geochronologic study of granulitized mafic eclogites and associated rocks from the footwall of the ADM yields important insights into the Mid- to Late-Miocene tectonic evolution of the Himalayan orogen. The mafic igneous precursor to the granulitized eclogites is 986.6 ± 1.8 Ma and was intruded into the paleoproterozoic (1799 ± 9 Ma) Ama Drime orthogneiss the latter being similar in age to rocks previously assigned to the Lesser Himalayan Series in the Himalayan foreland. The original eclogite-facies mineral assemblage in the mafic rocks has been strongly overprinted by granulite facies metamorphism at 750°C and 0.7-0.8 GPa. In the host Ama Drime orthogneiss, the granulite event is correlated with syn-kinematic sillimanite-grade metamorphism and muscovite dehydration melting. Monazite and xenotime ages indicate that the granulite

metamorphism and associated anatexis occurred at <13.2 ± 1.4 Ma. High-grade metamorphism was followed by post-kinematic leucogranite dyke emplacement at 11.6 ± 0.4 Ma. This integrated dataset indicates that high-temperature metamorphism, decompression and exhumation of the ADM post-dates mid-Miocene south-directed mid-crustal extrusion and is kinematically linked to orogen-parallel extension.

Keywords: **Himalaya, eclogite, granulite, metamorphism, uranium-thorium-lead geochronology, monazite.**

1. Introduction

Crustal rocks metamorphosed at high- to ultra-high pressure (HP – UHP) conditions provide important geodynamic constraints on the tectonic evolution of orogenic systems. Much of what is known about the behavior of continental crust during subduction, metamorphism and subsequent exhumation relies on petrological and geochronological studies of eclogites and granulites.

The Himalayan orogen is considered by many to be the type continent-continent collision zone. It is perhaps surprising then that compared with other orogens such as the Alps and the Urals eclogite-granulites are relatively rare. They are however known from at least three localities; two in the northwest Himalaya, (Tso Morari in Ladakh and Kaghan in NW Pakistan) [*Spencer et al.,* 1990; *Pognante and Spencer,* 1991; *Tonarini et al.,* 1993; *de Sigoyer et al.,* 1997, 2000; *Mukherjee and Sachan,* 2001; *O'Brien et al.,* 2001; *Kaneko et al.,* 2003; *Leech et al.,* 2005; *Guillot et al.,* 2008] and one in the central Himalaya (Ama Drime Massif, Fig. 1)[*Lombardo et al.,* 1998].

Both NW Himalayan eclogite localities reside in the Greater Himalayan Series (GHS) immediately to the south of the Indus suture zone [*Baldwin et al.,* 1998; *O'Brien et al.,* 2001] (Fig. 1) and are inferred to record remnants of Indian plate material subducted beneath Asia immediately following collision . The Kaghan Valley eclogites stabilized coesite, reaching peak metamorphic conditions of 725 ± 25ºC and 2.8-3.0 GPa [*O'Brien et al.* 2001 and references therein] at ~ 46 Ma [*Parrish et al.* 2006 and references therein]. The Tso Morari eclogites attained similar pressure-temperature (P-T) conditions [*Mukherjee and Sachan,* 2001 and references therein] at ~54 Ma [*de Sigoyer et al.* 2000; *Leech et al.* 2005].

In contrast, the Ama Drime granulitized eclogites, thus far the only eclogite occurrence documented from the central Himalaya, have received relatively little attention. *Groppo et al.* [2007] recognized four phases of metamorphism: an initial 'M1' eclogite facies event at >1.5 GPa and >580ºC; a peak granulite 'M2' event, at 0.8 – 1.0 GPa and >750ºC, a second granulitic 'M3' assemblage (Pl + Opx coronas around garnet) formed at lower P-T, ~0.4 GPa and 750ºC; and a final cooling, 'M4', stage at ~700ºC. *Lombardo and Rolfo* [2000] qualitatively assessed the timing of eclogite metamorphism as Tertiary. Two subsequent attempts to date the Ama Drime eclogites gave widely differing

interpretations. *Rolfo et al.* [2005] obtained three U-Pb zircon age components: 13-14 Ma, 88-110 Ma and ~1.8 Ga using the Sensitive High Resolution Ion Microprobe (SHRIMP) method. They suggested that the 13-14 Ma ages record the end of high-temperature, low-pressure fluid circulation, the Cretaceous ages represent the age of the mafic protolith of the eclogite while the Proterozoic ages were thought to be an inherited component. *Groppo et al.* [2007] inferred that the 13-14 Ma ages of *Rolfo et al.* [2005] dated their M3 granulite-facies event, but were unable to provide any direct evidence to support this hypothesis. *Liu et al.* [2007] dated three 'mafic granulite lenses' from the Kharta area that they inferred to be 'granulitized eclogites'. However, the exact location of the samples was unspecified, and from their Figure 2 (cross section) the lenses appear to reside within the GHS. These uncertainties notwithstanding, discordant U-Pb ID-TIMS zircon analyses with apparent $^{207}Pb/^{235}U$ ages ranging between ~350 Ma - 680 Ma with upper-intercept ages from 971 ± 8 Ma to 1122 ± 100 Ma, were interpreted by *Liu et al.* [2007] to record the protolith age of the mafic eclogites.

In spite of the limited and contradictory data available, the Ama Drime granulitized eclogites are crucial for reconstructing the tectonic history of the central Himalayan orogen. Not only do they potentially record early subduction of the Indian plate beneath Asia, but they also yield important information on the nature, timing and duration of metamorphism and extrusion of mid-crustal material from beneath the Tibetan plateau. Their protolith and lithotectonic association are equally important, especially as input into, as well as a means of testing, orogen-scale geodynamic reconstructions.

This study integrates structural observations of deformation (D), quantitative pressure-temperature estimates and U(-Th)-Pb geochronology on a variety of accessory phases (zircon, monazite, xenotime, titanite, rutile, uranothorite and thorium oxide) in an attempt to resolve the current discrepancies in assessments of the protolith age (Proteozoic versus Cretaceous), the overall structural setting, and the timing (t) of subsequent eclogite and granulite metamorphism and its relationship to anatexis, mid-crustal flow and exhumation. Our P-T-t-D dataset indicates that: 1) The protolith to the granulitized mafic eclogites is ~987 Ma while the host orthogneiss is ~1800 Ma; 2) that granulite metamorphism, melting and exhumation of the ADM, occurred <13 Ma, post-dating south-directed mid-crustal flow. These support recent models that proposed exhumation

of the ADM is a result of localized orogen-parallel (E-W) mid-crustal flow accommodated by north-south striking shear zones [*Jessup et al.,* 2008]. The data provide a means to reconcile previously disparate observations from the central Himalaya and yield new and important insight into the mid- late-Miocene evolution of the orogen.

2. Regional Geology

To the west and southwest of the ADM, the geology of the Everest region is comprised of three roughly parallel lithotectonic units that from structurally lowest to highest these include: the Lesser Himalayan Series (LHS); Greater Himalayan Series (GHS) and the Tibetan sedimentary sequence (TSS). These units are separated by three north dipping fault system; the Main Boundary Thrust (MBT), the Main Central Thrust zone (MCTZ) and the South Tibetan Detachment System (STDS) (Fig. 2).

The LHS, delimited at its base by the MBT and at its top by the MCTZ, consists of ~20 km structural-thickness of metamorphosed Precambrian-Mesozoic clastic sediments, overlain by mylonitic augen gneisses (Lesser Himalayan Crystallines) [*Brunel and Kienast,* 1986, *Schelling* 1992; *Brookfield* 1993; *Pognante and Benna* 1993].

The base of the GHS is marked by a ~5-km-thick high-strain zone containing a thrust system, the MCTZ (Fig. 1), and an inverted metamorphic sequence [Hubbard, 1989; Pognante and Benna 1993]. South of Mt. Everest, in the Dudh Kosi drainage, the maximum age for movement along the MCTZ is constrained by $^{40}Ar/^{39}Ar$ hornblende and $^{208}Pb/^{232}Th$ monazite geochronology and indicates that amphibolite-facies metamorphism of hanging-wall rocks occurred at 22 ± 1 Ma [*Hubbard and Harrison* 1989]; and potentially as early as 24-29 Ma [*Catlos et al.,* 2002].

The overlying GHS comprises a ~40-km-thick section of late Proterozoic to early Cambrian rocks [Parrish and Hodges *1996*] including metapelitic rocks, augen gneiss, calc-silicate and marble that have been metamorphosed to amphibolite to granulite facies during the Tertiary. Miocene age sills and dykes of crustal melt leucogranite intrude the GHS and at high structural levels culminate in large granite sills such as the Makalu and Nuptse granites [Searle *et al., 2003*; *Viskupic et al.,* 2005; *Jessup et al.,* 2008].

The P-T evolution of metamorphism in the GHS of Everest region is relatively well-constrained, with an early kyanite grade event (550 – 560°C and 0.8 - 1. 0 GPa) occurring

at least as early as 38.9 ± 0.9 Ma [*Cottle et al.,* in review], (often referred to as M1 [*Pognante and Benna* 1993; *Jessup et al.,* 2008]) being overprinted by a protracted higher temperature lower pressure sillimanite grade (650 - 750°C and 0.4 – 0.7 GPa) M2 [*Pognante and Benna* 1993] between ~28.0 – 22.6 Ma [*Simpson et al.,* 2000; *Viskupic et al.,* 2005; *Jessup et al.,* 2008*; Cottle et al.,* in review]. ^{40}Ar/^{39}Ar biotite ages from the GHS are consistently older than ~14 Ma suggesting that by this time metamorphism had ceased and the entire GHS had cooled through ~ 380°C [*Viskupic et al.,* 2005].

The upper margin of the GHS in the Everest region is bounded by a low-angle normal fault system, the STDS [*Burchfiel et al.,* 1992; *Carosi et al.,* 1998; *Carosi et al.,* 1999; *Murphy and Harrison,* 1999; *Searle*, 1999; *Searle et al.,* 2003; *Law et al.,* 2004; *Jessup et al.,* 2006; *Cottle et al.,* 2007] (Fig. 1, 2). This system comprises two major normal faults, the upper brittle Qomolangma Detachment (QD), which juxtaposes sedimentary rocks of the TSS with upper-amphibolite to lower-greenschist facies calc-silicate and schist of the Everest Series below, and the lower ductile Lhotse Detachment (LD), which places the Everest Series over upper-amphibolite facies sillimanite-cordierite bearing gneisses injected by leucogranite sills and dikes [*Searle*, 1999; *Searle et al.,* 2003; *Jessup et al.,* 2008] (Fig. 2, 3). To the northeast of Mt. Everest, in the Dzakaa Chu section the STDS forms a ~1000-m-thick zone of distributed ductile shear [*Cottle et al.,* 2007] (Fig. 2). Timing constraints on the STDS in the Everest area suggest that the upper brittle strands were active after 16 Ma, while the lower ductile system was active at 18-16 Ma [*Hodges et al.,* 1998; *Murphy and Harrison*, 1999; *Searle et al.,* 2003]. In the Dzakaa Chu section of the STDS (Fig. 2), U(-Th)-Pb dating of a leucogranitic dyke that cross-cuts the mylonitic fabric within the lower part of the STDS suggests that the majority of high-temperature ductile fabric development in this section of the shear zone occurred ≥20 Ma [*Cottle et al.,* 2007].

3. Geology of the Ama Drime Massif.

The Ama Drime Massif (ADM) (Fig. 2) lies to the northeast of the Mt. Everest Massif and forms a prominent ~ north-south-striking elongate region of elevated topography that extends ~70-km-northward across the crest of the High Himalaya. The ADM lies structurally beneath, and is separated from, the GHS package by two opposite-dipping

normal-sense shear zones, the Ama Drime detachment (ADD) system on the western limb and the Nyönno Ri detachment (NRD) on the eastern limb (Fig. 2) [*Jessup et al.,* 2008]. The structural geometry of the ADM is asymmetric with a moderately dipping western limb (ADD) and a more steeply dipping eastern limb (NRD) (Fig. 2). The consistency in fabric orientation and shear sense indicators between the high- to low-grade deformation within the ADD and NRD record a progression from ductile to brittle deformation [*Jessup et al.,* 2008]. The NRD offsets the STDS by ~20 km of apparent right-lateral separation (Fig. 1) and appears to define the western margin of the Xainza-Dinggyê rift [*Burchfiel et al.,* 1992; *Zhang and Lei,* 2007]. The fact that these younger features offset the STDS indicates that it is no longer capable of accommodating south-directed mid-crustal flow in this region [*Cottle et al.,* 2007; *Jessup et al.,* 2008].

The core of the ADM is largely composed of migmatitic orthogneiss (the Ama Drime orthogneiss) that contains a prominent foliation dipping west on the western limb, becoming sub-horizontal in the core and dipping to the east on the eastern limb, defining an overall elongate asymmetric north-south structural culmination [*Jessup et al.,* 2008] (Fig. 1). Mafic granulite lenses are common within the core of the ADM, are generally sub-parallel to the main tectonic foliation and are commonly boudinaged and rotated (Fig. 3). On the western limb of the ADM rotation of the mafic granulite lenses is largely a result of brittle faulting 'dominoeing' of the lenses during top-to-the-west shearing (Fig. 3b). Mafic layers are also offset by small-scale steeply west-dipping normal faults (Fig. 3c). Occasionally the lenses are cored by relatively fresh granulitized eclogites. Migmatitic gneiss that surrounds the mafic lenses records ductile fabric development that accommodated rotation of mafic lenses. Leucogranite dykes and sills, both pre- to syn-kinematic and post-kinematic, are common throughout the ADM (Fig 3a-b).

4. Petrology of mafic granulitized eclogites

In the areas that have been mapped so far, granulitized mafic eclogites are restricted to the footwall of the ADM, with petrographically similar rocks being widely distributed throughout the central region of the massif. The mafic rocks, ubiquitously hosted in felsic orthogneiss (Fig 3, 4a), range from tens of centimeter long boudins to elongate blocks several tens of metres in length (Fig. 3). The granulitized eclogites are dark green,

medium to coarse-grained rocks consisting of the mineral assemblage Grt + Cpx + Pl + Hbl + Bt + Qtz + Opx + Ilm (abbreviations after *Kretz*, [1983]) with accessory phases dominated by apatite with less abundant zircon, titanite, rutile and rare allanite (Fig. 5). Petrographically, AD43 consists of three distinct domains; 1) garnet with an associated Pl + Hbl + Opx ± Bt corona (Fig. 5a), 2) Cpx+Pl symplecitites (Fig. 5b) and 3) a coarse Hbl + Bt matrix (Fig. 5c). These domains are interpreted as relicts of eclogite-facies metamorphism that has been overprinted by a higher temperature granulite event. *Lombardo and Rolfo* [2000] and *Groppo et al.* [2007] also give accounts of rocks that are broadly similar to those described here.

4.1 Eclogite–facies metamorphism

Numerous quartz and rutile inclusions in the cores of garnet and Ca-rich regions (~35% Grossular content) of garnet (Fig. 5d) are the only record that is interpreted as evidence of the early prograde eclogite assemblage. Omphacite is absent from the matrix as well as inclusions in garnet. In the matrix, omphacite has been completely replaced by a fine-grained symplectite that contain intergrowths of Cpx + Pl with minor Opx and Hbl; exsolution-like sodic plagioclase makes up 27-32 volume % (Fig. 5c). Neither phengite nor its pseudomorphs were observed in any of the rocks examined during this study. *Groppo et al.* [2007] described the presence of high-Fe biotite and plagioclase symplectites in rocks from a similar location to the ones examined by this investigation and inferred them to be pseudomorphs after phengite (their Figures 3b and 4d). From the petrographic and textural data, it is inferred that the original eclogite mineral assemblage was dominated by a Ca-rich garnet + omphacite + amphibole. Pseudosection considerations and petrographic observations led *Groppo et al.* [2007] to infer P-T conditions of ~650°C and >1.2 GPa for the eclogite event.

4.2 Granulite –facies metamorphism

The peak metamorphic T assemblage that overprints the eclogite-facies assemblage includes Grt + Cpx + Opx + Pl + Ilm + Qtz and Pl + Cpx symplectites after omphacite (Fig. 5a,b,c). In contrast to the mafic rocks, diagnostic granulite-facies assemblages are absent in the felsic host orthogneisses. Thermobarometric estimates for the peak-T

granulite event employed the hornblende-plagioclase thermometers of [*Holland and Blundy*, 1994], the Grt-Opx thermometer of *Harley* [1984], the Grt-Cpx thermometer of *Powell* [1985], the Grt-Pl-Opx-Qtz geobarometer (linearised calibration of *Powell & Holland* 1988), and THERMOCALC (version 3.25; and the thermodynamic data set of *Holland and Powell,* 1998**).** Representative mineral analyses are given in (Table. 1). Because the granulite is silica-saturated, both edenite-richterite and edenite-tremolite hornblende-plagioclase thermometers were applied to AD43 and yield temperatures of ~753°C and 731°C respectively at a nominal pressure of 0.7 GPa. Grt-Cpx and Grt-Opx thermometers give similar temperature estimates of 704°C. Grt-Pl-Opx-Qtz equilibria yield a metamorphic pressure estimate of ~ 0.69 GPa. THERMOCALC run in Average P-T mode and using the same chemical data (Table 1) yielded P-T estimates of 0.79 ± 0.15 GPa and 769°C ± 124°C. In summary, both conventional geothermobarometry and THERMOCALC indicate that the peak-T granulite assemblage formed at 750°C ± 30°C and 0.7 - 0.8 GPa.

5. U(-Th)-Pb Geochronology

5.1 Analytical procedures

This study utilizes two complimentary analytical techniques, Isotope Dilution Thermal Ionization Mass Spectrometry (ID-TIMS) and Laser Ablation - Multi-Collector - Inductively Coupled Plasma Mass Spectrometery (LA-MC-ICPMS) to obtain U(-Th)-Pb isotopic data on a variety of accessory phases. Detailed analytical methods are outlined in Appendix 1. Analyses were conducted at the Natural Environment Research Council National Isotope Geoscience Laboratories (NIGL) at the British Geological Survey. A major component of this study was to combine *in-situ* polished thin section analyses with analyses on crystals separated by standard crushing, heavy liquid, and isodynamic magnetic separation techniques. Separated minerals were handpicked under ethanol, and only the highest quality grains were selected for analysis. Ages were calculated using the U decay constants of *Jaffey et al*. [1971], and the Th decay constant of *Amelin and Zaitsev* [2002]. Pbdat [*Ludwig,* 1993] and its Excel©-based derivative PbMacDat (http://www.earth-time.org/Pb_MacDat_5_1.xls) were used for ID-TIMS raw data reduction and an in-house Excel© spreadsheet for LA-MC-ICPMS data processing.

Calculated ages and data plots for both TIMS and LA-MC-ICPMS data were generated using Isoplot [*Ludwig,* 2003]. Tables 2-5 contain the full data sets. All errors in data tables and concordia plots are quoted at 2σ. Uncertainties on LA-MC-ICPMS data were propagated in the manner advocated by *Horstwood* [2008] and include a contribution from the external reproducibility of a reference material for the $^{206}Pb/^{238}U$, and $^{208}Pb/^{232}Th$ ratios as well as uncertainties in the U and Th decay constants. The external reproducibility of $^{206}Pb/^{238}U$ and $^{208}Pb/^{232}Th$ ratios is 3% (2σ) for U-Pb ratios and 4% (2σ) for Th-Pb ratios.

For monazite analyses an online common lead correction was performed using the calculated ^{204}Pb signal and an assumed common Pb ratio (e.g., that taken from *Stacy and Kramers* [1975] Pb evolution curve at the apparent age of the sample). The accuracy of the common-Pb correction was empirically estimated using several crystals of known $^{207}Pb/^{206}Pb$ ratio and different Pb concentrations. The reproducibility of the correction was then quadratically added to the internal error of the measured $^{207}Pb/^{206}Pb$ ratio.

In this study, both the U-Pb and Th-Pb isotope systems were used to date monazite. In the vast majority of analyses that are <50 m.y old, the $^{206}Pb/^{238}U$ ages are slightly older than the $^{208}Pb/^{232}Th$ ages. This reverse discordance is inferred to reflect incorporation of excess ^{230}Th during crystallization, leading to an excess of ^{206}Pb, a phenomenon commonly observed in young monazite [*Schärer,* 1984; *Parrish,* 1990]. Given that the Th-Pb system is unaffected by this disequilibrium, the $^{208}Pb/^{232}Th$ dates are taken as the most reliable estimates of the ages of these monazite grains (unless otherwise stated).

5.2 Samples

AD35 – Leucogranite cross-cutting eclogite body

AD35 is a Qtz + Kfs + Pl + Ms + Bt leucogranite dyke that fills a steeply-east-dipping normal-sense fault, which crosscuts a mafic eclogite lens and its host gneiss (Fig. 2, 3a-b). Microstructures indicate the dyke preserves its original igneous texture and lacks evidence for dynamic recrystallization. Based on these observations the age of this sample is interpreted to provide a minimum time constraint for: 1) HP metamorphism in the mafic eclogite, 2) ductile fabric development in the host gneisses and 3) top-to-the-west shearing in the western limb (ADD) of the Ama Drime Massif.

Backscattered electron (BSE), U (Fig. 6a), Y and Th mapping of monazite from AD35 defines distinct compositional variations between core and rim in most grains. Where possible, grains with rims larger than the ablation spot size (35µm diameter) were analyzed. However, due to the large number of grains with rims <20µm thick this was not always possible.

On a U-Pb concordia diagram (Fig. 7a) the laser-ablation analyses plot along a well-defined two component mixing line with a lower-intercept of 11.5 ± 5.2 Ma and an upper intercept of 1804 ± 11 Ma, mean squared weighted deviates (MSWD) [*Wendt and Carl,* 1991] = 2.8 (Fig. 8a). On a $^{208}Pb/^{232}Th$ - $^{206}Pb/^{238}U$ concordia diagram (Fig. 7b), six of the analyses cluster at the lower intercept of the discordia trajectory, are reversely discordant and lack isotopic evidence of an inherited component. Taking the weighted mean $^{208}Pb/^{232}Th$ of these six analyses yields an age of 11.6 ± 0.4 Ma with an MSWD close to unity (1.2). This is interpreted as crystallization age of the leucogranite dyke. The upper intercept age of 1804 ± 11 Ma is inferred to reflect a xenocrystic component and possibly the age of the melt-source material. The geologic significance of both age components is discussed below.

AD36 – Ama Drime Orthogneiss

Orthogneisses that are petrographically similar to AD36 are widespread throughout the ADM (Fig. 3 - 4a). AD36 is a Kfs + Qtz + Pl + Bt + Sil augen gneiss with a well-developed gneissic foliation defined by laths of biotite and fibrolite (Figs. 3, 4a). The gneiss samples lack any textural or mineralogical evidence of the high-pressure metamorphism as is preserved in the mafic boudins. The melanosome portion of the gneiss is composed of Bt + Qtz + Kfs + Sil + Pl, while the mm- to cm-thick, leucogranitic leucosomes make up ~40% of the rock and are composed of Kfs + Qtz + Sil ± Bt aggregates. Conjugate sets of melt-filled extensional (top-to-the east and top-to-the west) shear bands that are common in the gneiss (Fig. 4a) suggest that melting occurred syn-kinematically with respect to top-to-the-west shearing. Accessory phases are dominated by monazite, zircon, apatite, and xenotime (Fig. 6b-h).

Silllimanite-bearing leucosomes (Fig. 4a) are interpreted to have formed as a result of in-situ partial melting of the host meta-granitoid via a reaction such as:

Ms + Pl + Qtz = Sil + Kfs + melt (1)

To fully characterize the protolith as well as the metamorphic and magmatic history of this gneiss, accessory phases were analyzed by two complimentary methods (ID-TIMS and LA-MC-ICPMS). Zircons were extracted from a large (~5kg) sample using the techniques outlined above (Section 5.1). In addition, monazite and xenotime were analyzed directly in a standard polished section, allowing the age of the crystal to be related to a textural setting (leucosome versus melanosome) (Fig. 6g-h).

In this sample, zircon can be grouped into two distinct morphological populations: 1) large oscillatory-zoned euhedral crystals that occasionally contain thin rims (<5μm thick) that poikiloblastically enclose Qtz, Kfs, U-Th silicate and oxide as well as apatite (Fig. 6c); and 2) cloudy squat prisms with aspect ratios close to one (Fig. 6e-f). Zircon grains commonly contain cavities (Fig. 6e) as well as abundant inclusions of Qtz, Kfs and U-Th silicate and oxide (Fig. 6f). In sample AD36, the latter type of zircon is concentrated in the leucosomes, suggesting some petrogenetic-link to melt formation processes, while the euhedral crystals are more evenly distributed throughout the rock.

As with the leucogranite AD35, zircon, monazite and xenotime U(-Th)-Pb isotope data from AD36 define a well-defined two component mixing line with a lower intercept of 11.0 ± 3.3 Ma and an upper intercept of 1799 ± 12 Ma MSWD = 1.9 (Fig. 7c). Only one of the monazite analyses shows any inheritance with the other four clustering on, to slightly above, concordia (Figs. 7c-d). One of the monazites (009-1) is included within sillimanite (Fig. 7) and yields an $^{208}Pb/^{232}Th$ age of 13.2 ± 1.4 Ma (Fig. 7d), providing an upper limit on the timing of sillimanite-grade metamorphism and melting affecting of the Ama Drime orthogneiss. One xenotime has an apparent $^{206}Pb/^{238}U$ age of ~1700Ma while the other two analyses yield $^{206}Pb/^{238}U$ ages of 12.8 ± 0.4 Ma and 13.3 ± 0.5 Ma (Table 3). Combining the $^{208}Pb/^{232}Th$ ages of the four monazite grains yields a mean age of 12.7 ± 0.3 Ma MSWD = 1.9 is consistent with the xenotime ages and constrains the timing of melt crystallisation within the gneiss. The upper intercept of 1799 ± 12 Ma, predominantly defined by zircon with one xenotime analysis (Fig. 7c) suggests an early-Proterozoic age for the protolith granitoid. To resolve the origin of the poikiloblastic

texture observed in some zircons (e.g., Fig. 6c, e-f), several of the larger U-Th silicate and oxide inclusions were analyzed by the laser ablation technique. Only two crystals yielded reliable common-lead corrected $^{206}Pb/^{238}U$ ages of 10.0 ± 2.2 Ma and 12.0 ± 0.7 Ma (Table 3) and suggest that these grains, and hence the texture within which they are included, formed during in-situ melting of the gneiss.

Monazite-xenotime thermochronometry of AD36

The presence of coeval monazite and xenotime (see above) allows application of the monazite-xenotime geothermometer of *Gratz and Heinrich* [1997]. This thermometer relies on the equilibrium partitioning of Y between monazite and xenotime. In order to ensure the accuracy of this calibration, the analysed monazite and xenotime must be in chemical equilibrium during crystallization. Quantitative SEM-EDS analyses were confined to the young (~12 Ma) domains within dated monazite (Table 6; Fig. 6b), because they are the best candidates for fulfilling the equilibrium criteria. The thermometer also requires an independent pressure estimate, which unfortunately is not directly available for this rock. Instead, the textural and geochronlogical evidence (see above) and the growth of monazite rims during in-situ partial melting within the stability field of sillimanite are used. Available petrological data from the Himalaya suggest that this reaction occurs in the P-T range 0.8 – 1.0 GPa and ~750°C [e.g., *Inger and Harris,* 1992; *Harris and Massey,* 1994; *Vannay and Hodges,* 1996; *Harris et al.,* 2004]. Assuming that melting in AD36 occurred under similar pressure conditions, predicted Y_{Xmnz} temperatures for monazite rims range from 744 - 797ºC at 0.8 GPa to 710 - 763ºC at 1.0 GPa. If the assumed pressure conditions of monazite rim growth are reduced to ≤ 0.6 GPa, the resulting Y_{Xmnz} temperatures are >800ºC which would require an unreasonably high geotherm. The ~750ºC temperature obtained by this method is consistent with those obtained by conventional thermobarometry from the mafic granulitized eclogite (see above) and suggests that the best P-T estimate for the Ama Drime Orthogneiss at ~12.7 Ma is ~ 750ºC ± 30ºC and 0.7-0.8 GPa.

AD41 Migmatitic orthogneiss from hanging wall of Ama Drime detachment

Sample AD41 is from a ~1-km-thick package of orthogneiss lying in the immediate hanging wall of the ADD in the main Kharta valley on the western side of the ADM (Figs. 2, 4b). It appears to lie structurally within the Greater Himalayan Series (GHS), being overlain by Grt + Bt + Pl + Kfs + Qtz + Sil ± Crd ± Ky ± Rt metapelitic gneisses [*Borghi et al., 2003*; *Cottle et al.,* in review]. The sample is a banded migmatitic augen gneiss with a well-developed mylonitic S-C foliation defined by laths of biotite and fibrolite (Fig. 4b). The melanosome portion of the rock is composed of Bt + Sil + Qtz + Pl + Kfs while the cm-thick, syn-kinematic leucogranitic leucosomes comprise aggregates of Kfs + Qtz and rare biotite. Accessory phases are dominated by zircon, apatite and uranothorite, with the latter entirely restricted to the leucosomes. The leucosomes are inferred to have formed as a result of in-situ partial melting of the host meta-granitoid. This sample was selected for analyses to constrain whether variability exists in the protolith age of gneisses across the ADD as well as to link these ages to a previous geochronological investigation that constrained the timing of melt generation and metamorphism in the hanging wall rocks (GHS) [*Cottle et al.,* in review].

Zircon

Zircons from AD41 are generally large doubly terminated euhedral prisms with well-developed oscillatory growth zoning (Fig. 6i-j), occasionally preserving thin (1-3μm thick) rims with elevated U + Th content. 13 LA-MC-ICPMS U-Pb analyses were obtained from the oscillatory-zoned regions of the zircons (Fig. 7e). Several analyses show evidence of lead loss, with some additional analyses having a significant component of common lead. A discordia trajectory constructed through the zircon and uranothorite data (see below) (Fig. 7e) yield intercepts at 16 ± 20 Ma and 473 ± 16 Ma. The upper intercept age of 473 ± 16 Ma, MSWD 9.7 is interpreted to provide a crystallization age of the granitoid protolith (AD41).

Uranothorite

Doubly-terminated, euhedral to subhedral green translucent crystals that range from squat (2:1, length:width aspect ratio) to elongate (5:1) are common in the leucosomes of AD41

(Fig. 6k-l). The high concentration of uranium (18.5 – 26.2 wt % UO_2) in addition to thorium (52.1 – 57.8 wt% ThO_2) indicates that they are uranothorite as opposed to thorite *sensu-stricto*. The vast majority of grains examined contain inclusions of zircon, intergrowths of these two minerals were not observed and the uranothorite appears to have nucleated around zircon. Less common inclusions of quartz, K-feldspar, allanite and xenotime were also observed. Alteration is ubiquitous (e.g., Fig. 6l), however because of their high actinide concentration, a small analytical spot size (20µm diameter x 7µm deep) could be used to target pristine regions in the crystals.

Nine analyses were acquired from three crystals (Fig. 7f). One analysis (003-2) is significantly younger. On inspection after ablation the pit appears to have been partly located over a crack, suggesting that it may have been subjected to diffusive lead-loss (dashed ellipse on Fig 7f). Rejecting this one analysis, the eight remaining analyses yield a mean $^{206}Pb/^{238}U$ age of 15.8 ± 0.2 Ma with an MSWD = 0.9 (Fig. 7f). The fact that the uranothorites are restricted to leucosomes, along with their euheral morphology, suggests they formed during in-situ partial melting. The 15.8 ± 0.2 Ma age is therefore inferred to record the timing of melt generation in AD41.

AD43 - Mafic granulitized eclogite

Zircon, titanite and rutile (Fig. 8) were extracted from a large (~10kg) sample of granulitized eclogite (AD43) adjacent to the large mafic body in Figure 3a. Rutile, titanite and zircon from AD43 were dated with the intention of deciphering the protolith age as well as the timing of subsequent metamorphic events. Rutile (Fig. 8a) has a range of morphologies from acicular to sub-rounded crystals. Titanite forms colorless to light yellow subhedral discs 60 - 80µm long, occurring both as inclusions in garnet and within the matrix where it appears to have formed at the expense of rutile. Zircon in AD43 forms two distinct sub-populations (Fig. 8b-e). The dominant population comprises pink, translucent, doubly terminated euhedral crystals, many with elongate tubular melt inclusions and occasionally displaying oscillatory zoning in CL (Fig. 8c, e). The less abundant population of grains are small (<30µm diameter), colorless, euhedral, squat prisms (Fig. 8d). Although allanite was found in thin section, it was difficult to distinguish from the abundant amphibole and pyroxene in the separate.

Zircon analytical protocol followed a novel approach. Firstly, a selection of high quality, crack-free, pink-colored grains (Fig. 8b) was handpicked under alcohol using a binocular microscope. Grains were first washed thoroughly in alcohol and high-purity water and then mounted on double-sided sticky tape on the surface of a 1-inch diameter epoxy resin disc. The outer surfaces of the grains were initially rastered using a laser beam with a laser using a large spot size (100µm) at low fluence (~ 0.5mJ/cm^{-2}) to remove any surficial contamination. The grains were then analyzed by laser ablation using dynamic line rasters (Fig. 9a,b). The line rasters (X:Y:Z = 100µm x 15µm x 2µm) minimized penetration in the Z direction allowing the age of the potential 'rims' of the zircons highlighted in Cathodoluminescence (Cl) (Fig. 8e) to be determined; a critical step that is impossible when analyzing crystals with thin (<20µm) rims set in polished grain mounts or by conventional dissolution techniques. A selection of crystals was also dated using static spot analyses that penetrated ~25µm into the grain, providing isotopic information on the core of the grains (Fig. 9c). Finally, selected crystals were removed from the tape, washed again, and analyzed by ID-TIMS following the method outlined above (section 5.1).

5.4 LA-MC-ICPMS

Zircon

Dynamic line rasters on the outer surfaces of five grains consistently yield discordant U-Pb data that define a lead-loss array with an upper intercept of 1004 ± 35 Ma, MSWD = 0.9 (Fig. 10a). Fifteen spot analyses also yield discordant data with an upper intercept of 1004 ± 23 Ma, MSWD = 0.6 (Fig. 10b). Both these ages are within error of each other and the ID-TIMS result (see below), and suggest that the cores and rims of the zircons probably record growth during a single thermal event. Alternatively, it is possible that multiple ages are recorded within the zircon that are smaller than the analytical resolution (~3 - 4% 2σ) of the LA-MC-ICPMS technique. This interpretation appears less plausible given the overall consistency of the dataset across multiple analytical techniques.

Despite selection of the highest quality grains, the line raster and spot analyses suffer from significant amounts of lead loss, the magnitude of which appears to be generally greater on the surfaces of the grains than in the interiors. Nevertheless, the external

reproducibility of the $^{207}Pb/^{235}U$ ratios on individual spot and line analyses is ~4% and 6% (2σ) respectively, comparable in precision to spot ablations in polished grain mounts. This indicates that the surface ablation method provides both an ideal way to quickly acquire reconnaissance data with minimal preparation and is a useful tool for analyzing thin rims (<10μm) that are otherwise beyond the spatial resolution of in-situ dating methods (e.g., Secondary Ionisation Mass Spectrometry (SIMS) or SHRIMP).

5.5 ID-TIMS

Zircon

Six single grain fractions each of the pink elongate and squat crystals were analyzed by ID-TIMS. Of the pink zircon grains, one fraction is sub-concordant, with the rest between 1% and 13% normally discordant. All six analyses define a linear lead-loss trajectory with an upper intercept age of 986.6 ± 1.8 Ma and a lower intercept age of 172 ± 38 Ma MSWD 0.1 (Fig. 11a). The six squat crystals are generally more discordant yielding a poorly defined lead loss array with an upper intercept of 970 ± 40 Ma and a lower intercept of 440 ± 180 Ma MSWD 20 (Fig. 11a). The presence of elongate inclusions inferred to be melt (Fig. 9c) and regular oscillatory zoning (Fig.8c) both provide evidence for a magmatic origin for the pink zircon grains. Therefore the 986.6 ± 1.8 Ma age is interpreted as the best estimate for the timing of crystallization of the magmatic precursor to the granulitized eclogites.

Titanite

Four titanite fractions containing between 25 and 31 crystals each, representing the variation in population morphology, were analyzed. The common lead content of the titanite is very high; with the radiogenic lead to common lead ratio (Pb^*/Pb_c) consistently around 0.03. The low lead concentration, high common lead content and limited variation in the Pb/Pb and Pb/U ratios (Fig. 12b-c) combine to make calculating a geologically meaningful age extremely difficult these data were not pursued further.

Rutile

Eight analyses each containing between 30 and 45 crystals were measured. Rutile crystals are low in both U (3 - 12ppm) and Pb (~0.1ppm) and have Pb^*/Pb_c ratios of around 0.1 (Table 5). The analyses corrected for spike, blank (the isotopic composition of which is very similar to Stacey-Kramers model Pb at 0-50 Ma) and mass fractionation only (i.e., not common lead corrected) are plotted on a conventional isochron diagram (Fig. 11b) and a Tera-Wasserburg concordia plot (Fig. 11c). Both plots indicate significant scatter in the data with six analyses forming an array with $^{206}Pb/^{204}Pb$ ratios of between 23 and 40 while analyses 13 and 17 are more radiogenic with $^{206}Pb/^{204}Pb$ ratios of 117 and 123 respectively. As a first order approximation these data are treated as mixtures of radiogenic and common lead. To identify the isotopic composition of potential common lead reservoir(s) within AD43, the $^{207}Pb/^{206}Pb$ and $^{206}Pb/^{204}Pb$ ratios of low-K plagioclase feldspar in AD43 were measured directly in a polished thin section by LA-MC-ICPMS. The resulting analyses have $^{207}Pb/^{206}Pb$ ratios of 0.87 ± 0.02, $^{207}Pb/^{204}Pb$ ratios of 15.8 ± 1.0 and $^{206}Pb/^{204}Pb$ ratios of 18.2 ± 0.8 (2σ).

Taking the main array of data (analyses 14, 15, 16, 18, 19 20) and constructing a discordia trajectory anchored using the appropriate feldspar values yields an apparent age of ~16Ma but with an MSWD of >>100. The excess scatter indicates that these rutiles are not a co-genetic population. Isochrons for analyses 17 and 13 have much older implied ages of 185 and 48 Ma, respectively. A minimum calculated age includes analysis 20 tied to the feldspar initial composition, with an age of 14 ± 0.2 Ma. The large spread in calculated ages from ~14 Ma to ~185 Ma and the lack of coherence implies a one or more of (1) a complex mixture of rutile formation ages with a potentially variable amount of Pb loss; (2) the presence of tiny amounts of older zircon contained within younger or at least reset rutile. Inclusions of zircon were not observed though they cannot be entirely ruled out, but if this is the explanation they must be present in most of the analyses to generate the scatter. Alternatively, if this is not the explanation, then the data imply that rutile consists of variable amounts of an old (>185 Ma) rutile component variable reset and/or variably mixed with a younger (~14 Ma or slightly younger) rutile component.

6. DISCUSSION

6.1 Geochronology data

Ama Drime Orthogneiss and Leucogranite dyke

Accessory phases in the Ama Drime orthogneiss (AD36) record two events, the ~1800 Ma emplacement of the protolith granitoid (defined by zircon, monazite and xenotime) and an in-situ partial melting event at ~13 Ma (defined by monazite, xenotime and thorium oxide) under P-T conditions of 750°C ± 30°C and 0.7 - 0.8 GPa. The similarity between the protolith age of the gneiss and the xenocrystic monazite in the leucogranite (AD35) provide evidence that in-situ partial melting of a granitic source can produce leucogranitic melts. Furthermore, these results suggest that Himalayan leucogranites may not be derived solely from Greater Himalayan pelitic protoliths as emphasized by some previous workers [e.g., *Harris and Massey,* 1994].

The Ama Drime orthogneiss is similar in age to numerous early-mid Proterozoic augen gneisses within the GHS and LHS that have been described throughout the Himalayan orogen. In NW India, orthogneisses within the LHS have been dated at between ~1840 - 1860 Ma [Miller et al., 2000 and references therein]. In Eastern Bhutan, *Daniel et al.* [2003] dated a quartzofeldspathic gneiss from the LHS several hundred meters structurally below the MCT. As well as a ~20 Ma metamorphic overprint, they obtained ages of 1760-1840 Ma from zircon and 1760 ± 7 Ma from monazite. Richards et al. [2006] obtained a similar age of 1790 ± 3 Ma for a metarhyolite from the LHS of Bhutan. In Nepal, the Ulleri augen gneiss has been dated by U-Pb zircon at ~1831 Ma [*DeCelles et al.,* 2000]. In the Dudh Kosi drainage south of Mt. Everest, *Catlos et al.* [2002] reported SHRIMP $^{208}Pb/^{232}Th$ ages as old as 1566 ± 49 Ma (1σ) from monazite in the Phaplu augen gneiss (LHS), a unit interpreted by these workers to be a structural equivalent of the Ulleri augen gneisses (LHS) outcropping further to the east.

Considerable debate exists regarding the lithotectonic association of a number of orthogneisses in Nepal and, in particular, whether they belong to the LHS [e.g., *DeCelles et al.,* 2000; *Robinson et al.,* 2001; *Catlos et al.,* 2002] or the GHS [e.g., *Searle et al., 2003*; *Goscombe et al.,* 2006]. The dispute centers on different field-based interpretations of the Phaplu - Ulleri augen gneisses as either in the footwall of the MCTZ, thus making them part of the LHS [e.g., *DeCelles et al.,* 2000; *Robinson et al.,*

2001; *Catlos et al.,* 2002] or in the hanging wall of the MCTZ, making them part of the GHS [e.g.*, Searle et al.,* 2003; *Goscombe et al.,* 2006].

Accurately assigning the Ama Drime orthogneiss to either the LHS or GHS is important for understanding the kinematic history of the MCTZ. However, this requires: 1) constraints on the structural, stratigraphic and lithological continuity (or lack thereof) between the Ama Drime orthogneiss as exposed on the Ama Drime range in Tibet and gneisses near the MCTZ towards the south exposed in the Arun River gorge in Nepal; 2) detailed assessment of the relative merits of the conflicting structural interpretations of the Phaplu - Ulleri augen gneisses with respect to the location of the MCTZ.

Regarding 1) - the area to the south of the Ama Drime is extremely poorly mapped with virtually no age control available. Furthermore, the little data that are available yield significant differences in the interpretation of the location of the MCTZ and the surrounding rock units [*c.f. Bordet,* 1961 and *Goscombe et al.,* 2006]. Regarding 2) – although the location and definition of the MCTZ, is a perennial issue in Himalayan tectonics, an assessment of the relative interpretations outlined above is the subject of much debate [e.g., *Searle et al*., 2002; *Kohn et al.,* 2002] and is beyond the scope of this work.

In light of these two major limiting issues, the Ama Drime orthogneiss is not directly assigned a GHS or LHS affinity. It is simply noted that this 1800 Ma orthogneiss (AD36) is very similar in age to the Proterozoic Ulleri-Phaplu gneisses that outcrop in the Himalayan foreland to the southwest of the ADM.

Sillimanite-grade in-situ partial melting of the Ama Drime orthogneiss occurred syn-kinematically with respect to normal-sense ductile deformation as evidenced by the presence of melt-filled extensional shear bands (≤13.2 ± 1.4 Ma). A crosscutting leucogranite dyke (11.6 ± 0.4 Ma) provides a maximum age for ductile deformation and associated fabric development in the core of the ADM. This dyke occupies a steeply inclined fault with apparent top-down-to-the-west displacement, and is inferred to be synchronous with brittle deformation. The consistency in top-to-the-west shear in both high-temperature deformation features (e.g., melt-filled extensional shear bands) and brittle features (e.g., steeply dipping faults) suggests that deformation of these rocks along with those within the western limb occurred during orogen parallel extension. Field

and geochronologic evidence suggests that syn-kinematic melt in the host orthogneiss was mobilized into leucogranite dykes, over a very short time span of around 1-2 m.y.. This implies that that late-stage decompression and exhumation of the ADM during orogen-parallel extension occurred extremely rapidly at ~13-12 Ma. Combining the high-temperature P-T-t data presented here with low-temperature (U-Th)/He apatite thermochronometry from *Jessup et al.* [2008], it is possible to tentatively estimate a cooling rate of 66 ± 1°C / Ma and an exhumation rate of 2.2 ± 0.2mm/yr for the period ~13 Ma to ~2 Ma (time of cooling through ~70-90°C from (U-Th)/He apatite data). This is consistent with *Jessup et al.* [2008] who proposed that the locus of exhumation migrated into the footwall block between 12-13 Ma and that the ADM was exhumed at a minimum rate of ~1 mm/yr between 1.5 and 3 Ma.

AD41 Greater Himalayan Series gneiss

The 473 ± 16 Ma U-Pb zircon protolith age of AD41 is comparable to other gneisses within the GHS such as the 465 - 470 Ma Namche Orthogneiss in the Everest region [*Viskupic and Hodges,* 2001], a 484 ± 9 Ma a "Formation III augen gneiss" in the Annapurna Region [*Godin et al.,* 2001], and numerous other Cambro-Ordovician orthogniesses that form part of a discontinuous belt extending 1800-km-along-strike from west (Zanskar) to east (Bhutan) [*Cawood et al.,* 2007]. This age, along with previous mapping, petrology and geochronology (*Cottle et al.,* in review) confirms that the immediate hanging wall of the ADD is most likely to be part of the GHS. Additionally, the considerable difference in protolith ages of orthogneisses across the ADD implies that it is a major structure responsible for juxtaposing two distinct lithotectonic units. The early history of ADD, and in particular whether it represents a reactivated early thrust fault, remains unclear, and in our view cannot be substantiated until the area to the south of the ADM has been mapped in detail.

In-situ partial melting of AD41 occurred at 15.8 ± 0.2 Ma, pre-dating texturally equivalent melt generation in the footwall gneisses by ~2 Ma. This age is also consistent with early melt generation at structurally higher levels within the GHS [*Cottle et al.,* in review].

Granulitized Mafic Eclogite - Zircon

The LA-MC-ICPMS and ID-TIMS data presented here indicate that the protolith of the granulitized mafic eclogites in the ADM (AD43) is mid-late proterozoic (986.6 ± 1.8 Ma), ruling out the possibility that these rocks were part of the Cretaceous Rajmahal Traps [*Rolfo et al.*, 2005]. In addition, this age appears not to correlate with other mafic rocks, either within the Himalayan orogen itself or in the north Indian cratonic basement.

A speculative correlation exists with the Eastern Ghats province in southeast India. In this region, geochronological studies (see Veevers, [2007] and references therein for a summary) suggest that granulite facies metamorphism and intrusion of rocks of broadly granitoid composition occurred ~ 980 Ma. This belt has been linked to the Ryder Bay complex in East Antarctica [*Fitzsimons*, 2000 and references therein], with both forming part of a large-scale Grenville-age tectonic province. However, despite the temporal correlation it remains unclear whether the mafic rocks in the ADM are directly related to felsic intrusive rocks in the Eastern Ghats or whether they represent two disparate events within the large-scale Grenville tectonic system.

Several reports exist of ~980 m.y. old detrital zircons from the three main lithotectonic zones throughout the Himalayan orogen (LHS, GHS, TSS) [e.g., *Parrish and Hodges*, 1996; *DeCelles et al.,* 2000; *Myrow et al.,* 2003 and references therein; *Martin et al.,* 2005; *Gehrels et al.,* 2006a, 2006b; *Richards et al.,* 2006; *Cawood et al.,* 2007]. Although it is tempting to draw correlations between the granulitized eclogites and detrital zircons from the various lithotectonic zones, a genetic link between the two is purely speculative and a robust test of this hypothesis would require significantly more data (e.g., trace element, Hf and/or O isotopic data from zircon).

Granulitized Mafic Eclogite - Rutile

A unique interpretation of the rutile data for AD43 is elusive but it would appear that a younger component of rutile, whether formed at ~14 Ma or finally closed to diffusion at about 14 Ma, is present in this sample**.** This age overlaps with the timing of granulite facies metamorphism (750°C ± 30°C and 0.7 - 0.8 GPa) in the host Ama Drime orthogneiss constrained to have occurred at ≤13.2 ± 1.4 Ma.

Traditionally, rutile has been viewed as a mineral with a closure temperature for Pb diffusion of ~400-450°C (e.g. *Mezger et al.,* [1989]) though this can be higher with rapid cooling and/or larger effective diffusion radius (e.g. *Cherniak* [*2000*]). Given the much higher granulite facies temperatures experienced at about this time, even with rapid cooling it is unlikely that much older rutile ages could be preserved without being fully armoured by a stable mineral (i.e. garnet). We have inspected the rutiles for zircon inclusions by making a specific highly polished grain mount of internal sections and have failed to observe such inclusions. Therefore, the preservation of older rutile ages, partially reset, requires an explanation.

Another plausible way to explain this rutile dataset is for their formation taking place perhaps >900 Ma during a granulite event, followed by a long period of lower temperatures preserving such old ages; this would then be followed by an abrupt heating episode to granulite facies around ~13-14 Ma causing significant to near-complete Pb loss and possible formation of new rutile. This option, though controversial, is consistent with the data as presently understood. The implication is that the rocks of the ADM may have not experienced the more protracted and composite metamorphic history of the overlying GHS, and that the ADM may have only been incorporated in the tectonic collage of the GHS at a very late stage. The lack in the ADM of any evidence of early Miocene metamorphism similar to that seen in the GHS is consistent with this interpretation.

6.2 Tectonic Implications

From ~39 Ma until ~16 Ma the tectonic evolution of the core of the Himalayan orogen was dominated by synchronous movement on two north-dipping, yet opposite shear sense, fault systems (the MCTZ and STDS). This coeval movement facilitated south-directed flow of mid-crustal material (the GHS) from beneath the Tibetan plateau southward toward the Indian foreland (see *Godin et al.* [2007] and references therein for a summary). $^{40}Ar/^{39}Ar$ biotite ages suggest that the GHS, at least in the Everest region, had cooled through ~380°C by 14 Ma [*Viskupic et al.,* 2005] implying that orogen-scale coupling of the STDS-MCTZ system and associated ductile flow must have ceased by this time. Clearly then, granulite facies metamorphism and in-situ anatexis at <13 Ma,

melt mobilization at ~11.6 Ma and subsequent exhumation of the ADM must post-date this south-directed flow and cannot therefore be genetically linked with it. Instead, we propose an alternative hypothesis - that at ~13 Ma a fundamental shift occurred in the dynamics of this part of the Himalayan system; from south-directed flow of mid-crustal rocks bounded by north dipping faults as recorded by the MCTZ-GHS-STDS system to orogen-parallel crustal-scale E-W extension accommodated by north-south striking fault systems [*Jessup et al.,* 2008]. Extension in the upper crust was manifested as north-south striking graben and brittle normal faults, while young metamorphic culminations such as the ADM record high-temperature ductile metamorphism, melting and exhumation of the mid-crust that was accommodated by large-scale north-south striking normal-sense ductile shear zones [*Jessup et al.,* 2008]. The data presented in this paper provide the first direct timing constraints on the minimum timing of the initiation of orogen-parallel mid-crustal flow along the southern margin of the Tibetan Plateau.

As highlighted by *Groppo et al.* [2007] the major difference between the NW Himalayan eclogites and those in the ADM lies not in the pressure conditions of peak metamorphism, but in the path followed by the rocks during their subsequent exhumation. In the NW Himalaya, after initial subduction of the leading edge of the Indian plate to depths approaching 80km, the resulting eclogites were exhumed along a cooling path at close to plate velocity rates [*Parrish et al.,* 2006]. They, therefore, reached relatively shallow mid-crustal positions without having undergone a major retrogressive high-temperature metamorphic event. They were thus largely unaffected by later stages of extrusion and exhumation related to south-directed mid-crustal flow of the GHS. In contrast, after eclogite-facies metamorphism, the ADM granulitized eclogites were thoroughly overprinted by a high T granulite event, presumably as a result of longer residence time in the mid-crust, ultimately caused by much slower rates of initial exhumation and a delay in final exhumation until <13 Ma during E-W extension.

7. Summary

This investigation presents U(-Th)-Pb geochronologic data that constrain the metamorphic and magmatic evolution of the Ama Drime Massif. The ADM is cored by the Ama Drime orthogneiss with a Paleoproterozoic (1799 ± 9 Ma) protolith age, which

were intruded by mafic magmas at 986.6 ± 1.8 Ma. This package of rocks was subducted to depths of at least 50km, stabilizing omphacite in the mafic lithologies. The eclogite-facies assemblage was overprinted by syn-kinematic granulite-facies metamorphism that approached 750°C ± 30°C and 0.7 - 0.8 GPa, is associated with in-situ anatexis in the host gneiss and rapid exhumation of the ADM. Monazite and xenotime constrain the granulite and anatectic event to have occurred at 13.2 ± 1.4 Ma. Metamorphism was followed by post-kinematic leucogranite dyke emplacement at 11.6 ± 0.4 Ma. High-T metamorphism, anatexis and exhumation of the ADM appears to post-date broadly equivalent events in the structurally overlying GHS, suggesting that this region records a fundamental transition from south-directed to orogen-parallel mid-crustal flow and exhumation that was accommodated by north-south striking normal-sense crustal-scale shear zones (ADD and NRD). The ADM provides an important window into mid-crustal processes that characterized the mid-late Miocene evolution of the Himalaya.

Acknowledgements

This work was funded by a New Zealand Tertiary Education Commission Doctoral Scholarship (TAD 1433) awarded to Cottle and a Geological Society of America research grant and a 2010 Fellowship from the College of Science at Virginia Tech to Jessup. Isotopic analyses were made possible through a Natural Environment Research Council NIGFSC grant (IP/846/0505).

References

Amelin, Y. and A. N. Zaitsev (2002), Precise geochronology of phoscorites and carbonatites: The critical role of U-series disequilibrium in age interpretations, Geochim. Cosmochim. Acta, 66(13), 2399-2419.

Baldwin, J. A., K. V. Hodges, S. A. Bowring, M. W. Martin, H. K. Sachan, and S. De J. (1998), Continental subduction in the western Himalayan Orogen?, Abstracts with Programs - Geological Society of America, 30(7), 269.

Bordet, P. (1961), Recherches Geologiques Dans l'Himalaya Du Nepal, Region Du Makalu, 275 pp., CNRS, Paris.

Borghi, A., D. Castelli, B. Lombardo, and D. Visoná (2003), Thermal and baric evolution of garnet granulites from the Kharta region of S Tibet, E Himalaya, European Journal of Mineralogy, 15(2), 401-418.

Burchfiel, B. C., Z. Chen, K. V. Hodges, Y. Liu, L. H. Royden, C. Deng, and J. Xu (1992), The South Tibetan Detachment System, Himalayan Orogen; Extension Contemporaneous with and Parallel to Shortening in a Collisional Mountain Belt, vol. 269, 41 pp., Geological Society of America, Boulder, CO, United States.

Brookfield, M. E. (1993), The Himalayan Passive Margin from Precambrian to Cretaceous Times, Sediment. Geol., 84(1-4), 1-35.

Brunel, M. and J. R. Kienast (1986), Petro-Structural Study of Himalayan Ductile Thrusts as seen in the Everest-Makalu Transversal (Western Nepal), Canadian Journal of Earth Sciences, 23(8), 1117-1137.

Carosi, R., B. Lombardo, G. Molli, G. Musumeci, and P. C. Pertusati (1998), The south Tibetan detachment system in the Rongbuk valley, Everest region. Deformation features and geological implications, Journal of Asian Earth Sciences, 16(2-3), 299-311.

Carosi, R., B. Lombardo, G. Musumeci, and P. C. Pertusati (1999), Geology of the Higher Himalayan Crystallines in Khumbu Himal (Eastern Nepal), Journal of Asian Earth Sciences, 17(5-6), 785-803.

Catlos, E. J., T. M. Harrison, C. E. Manning, M. Grove, S. M. Rai, M. S. Hubbard, and B. N. Upreti (2002), Records of the evolution of the Himalayan orogen from in-situ Th-Pb ion microprobe dating of monazite: Eastern Nepal and western Garhwal, Journal of Asian Earth Sciences, 20(5), 459-479.

Cawood, P. A., M. R. W. Johnson, and A. A. Nemchin (2007), Early palaeozoic orogenesis along the Indian margin of Gondwana: Tectonic response to Gondwana assembly, Earth Planet. Sci. Lett., 255(1-2), 70-84.

Cherniak, D. J. (2000), Pb diffusion in rutile, Contributions to Mineralogy and Petrology, 139(2), 198-207.

Corfu, F. and E. C. Grunsky (1987), Igneous and Tectonic Evolution of the Batchawana Greenstone-Belt, Superior Province - a U-Pb Zircon and Titanite Study, J. Geol., 95(1), 87-105.

Corfu, F. and S. R. Noble (1992), Genesis of the southern Abitibi greenstone belt, Superior Province, Canada: evidence from zircon Hf isotope analyses using a single filament technique, Geochimica et Cosmochimica Acta, 56(5), 2081-2097.

Cottle, J. M., M. J. Jessup, D. L. Newell, M. P. Searle, R. D. Law, and M. S. A. Horstwood (2007), Structural insights into the early stages of exhumation along an orogen-scale detachment: The South Tibetan Detachment System, Dzakaa Chu section, Eastern Himalaya, Journal of Structural Geology, 29(11), 1781-1797.

Cottle, J.M., M. P. Searle, S. R. Noble, M. S. A. Horstwood, R.R. Parrish (In review). Dating the timing and duration of channel flow in the Mt. Everest region. Submitted to the Journal of Geology.

Daniel, C. G., Hollister, L. S., Parrish, R. R. & Grujic, D. 2003. Exhumation of the Main Central Thrust from lower crustal depths, eastern Bhutan Himalaya. Journal of Metamorphic Geology 21, 317-334.

Davis, W. J., V. J. McNicoll, D. R. Bellerive, K. Santowski, and D. J. Scott (1997), Modified chemical procedures for the extraction and purification of uranium from titanite, allanite, and rutile in the Geochronology Laboratory, Geological Survey of Canada: In: Radiogenic age and Isotopic Studies, Report 10; Geological Survey of Canada, Current Research 1997-F, 33-35.

DeCelles, P. G., G. E. Gehrels, J. Quade, and T. P. Ojha (1998), Eocene early Miocene foreland basin development and the history of Himalayan thrusting, western and central Nepal, Tectonics, 17(5), 741-765.

DeCelles, P. G., G. E. Gehrels, J. Quade, B. LaReau, and M. Spurlin (2000), Tectonic implications of U-Pb zircon ages of the Himalayan orogenic belt in Nepal, Science, 288(5465), 497-499.

de Sigoyer, J., S. Guillot, J. M. Lardeaux, and G. Mascle (1997), Glaucophane-bearing eclogites in the Tso Morari dome (eastern Ladakh, NW Himalaya), European Journal of Mineralogy, 9(5), 1073-1083.

de Sigoyer, J., V. Chavagnac, J. Blichert-Toft, I. M. Villa, B. Luais, S. Guillot, M. Cosca, and G. Mascle (2000), Dating the Indian continental subduction and collisional thickening in the northwest Himalaya: Multichronology of the Tso Morari eclogites, Geology, 28(6), 487-490.

Fitzsimons, I. C. W. (2000), A review of tectonic events in the East Antarctic Shield and their implications for Gondwana and earlier supercontinents, J. Afr. Earth Sci., 31(1), 3-23.

Gratz, R. and W. Heinrich (1997), Monazite-xenotime thermobarometry: Experimental calibration of the miscibility gap in the binary system $CePO_4$-YPO_4, Am. Mineral., 82(7-8), 772-780.

Gehrels, G. E., P. G. DeCelles, T. P. Ojha, and B. N. Upreti (2006a), Geologic and U-Pb geochronologic evidence for early Paleozoic tectonism in the Dadeldhura thrust sheet, far-west Nepal Himalaya, Journal of Asian Earth Sciences, 28(4-6), 385-408.

Gehrels, G. E., P. G. DeCelles, T. P. Ojha, and B. N. Upreti (2006b), Geologic and U-Th-Pb geochronologic evidence for early Paleozoic tectonism in the Kathmandu thrust sheet, central Nepal Himalaya, Geological Society of America Bulletin, 118(1-2), 185-198.

Godin, L., R. R. Parrish, R. L. Brown, and K. V. Hodges (2001), Crustal thickening leading to exhumation of the Himalayan metamorphic core of central Nepal; insight from U-Pb geochronology and $^{40}Ar/^{39}Ar$ thermochronology, Tectonics, 20(5), 729-747.

Godin, L., Grujic, D., Law R D, and Searle, M.P., 2006, Channel flow, ductile extrusion and exhumation in continental collision zones; an introduction: Geological Society Special Publications 268:1-23.

Goscombe, B., D. Gray, and M. Hand (2006), Crustal architecture of the Himalayan metamorphic front in eastern Nepal, Gondwana Research, 10(3-4), 232-255.

Groppo, C., B. Lombardo, F. Rolfo, and P. Pertusati (2007), Clockwise exhumation path of granulitized eclogites from the Ama Drime range (Eastern Himalayas), J. Metamorph. Geol., 25(1), 51-75.

Guillot, S., G. Mahéo, J. de Sigoyer, K. H. Hattori, and A. Pêcher (2008), Tethyan and Indian subduction viewed from the Himalayan high- to ultrahigh-pressure metamorphic rocks, Tectonophysics, 451(1-4), 225-241.

Harris, N. B. W. and J. A. Massey (1994), Decompression and anatexis of Himalayan metapelites, Tectonics, 13(6), 1537-1546.

Harris, N. B. W., M. Caddick, J. Kosler, S. Goswami, D. Vance, and A. G. Tindle (2004), The pressure-temperature-time path of migmatites from the Sikkim Himalaya, J. Metamorph. Geol., 22(3), 249-264.

Hodges, K. V., M. S. Hubbard, and D. S. Silverberg (1988), Metamorphic constraints on the thermal evolution of the central Himalayan Orogen, Philosophical Transactions of the

Royal Society of London, Series A: Mathematical and Physical Sciences, 326(1589), 257-280.

Holland, T.J.B., and Blundy, J., 1994, Non-ideal interactions in calcite amphiboles and their bearing on amphibole-plagioclase thermometry: Contributions to Mineralogy and Petrology, v. 116, p. 433-447.

Holland, T. J. B. and R. Powell (1998), An internally consistent thermodynamic data set for phases of petrological interest, J. Metamorph. Geol., 16(3), 309-343.

Horstwood, M. S. A., G. L. Foster, R. R. Parrish, S. R. Noble, and G. M. Nowell (2003), Common-Pb corrected in-situ U-Pb accessory mineral geochronology by LA-MC-ICP-MS, J. Anal. At. Spectrom., 18(8), 837-846.

Horstwood, M.S.A (2008), Data reduction strategies, uncertainty assessment and interpretation of LA–(MC–)ICP–MS isotope data. In: Laser Ablation ICP-MS in the Earth Sciences: Current Practices and Outstanding issues (P. Sylvester ed.) Mineral. Soc. Can. Short Course Series 40, 283-303.

Hubbard, M. S. (1989), Thermobarometric Constraints on the Thermal History of the Main Central Thrust Zone and Tibetan Slab, Eastern Nepal Himalaya, J. Metamorph. Geol., 7(1), 19-30.

Hubbard, M. S. and T. M. Harrison (1989), $^{40}Ar/^{39}Ar$ age constraints on deformation and metamorphism in the Main Central Thrust zone and Tibetan Slab, eastern Nepal Himalaya, Tectonics, 8(4), 865-880.

Inger, S. and N. B. W. Harris (1992), Tectonothermal Evolution of the High Himalayan Crystalline Sequence, Langtang Valley, Northern Nepal, J. Metamorph. Geol., 10(3), 439-452.

Jaffey, A. H., K. F. Flynn, L. E. Glendenin, C. R. Bentley, and A. M. Essling (1971), Precision measurements of half-lives and specific activities of 235U and 238U., Physics Reviews, C4, 1889-1906.

Jessup, M. J., Law R D, M. P. Searle, and M. S. Hubbard (2006), Structural evolution and vorticity of flow during extrusion and exhumation of the Greater Himalayan Slab, Mount Everest Massif, Tibet/ Nepal; implications for orogen-scale flow partitioning, Geological Society Special Publications, 268, 379-413.

Jessup, M.J., Cottle, J.M., Searle, M.P., Law, R.D., Tracy, R.J., Newell, D.L. & Waters, D.J. (*2008*) P-T-t-D paths of Everest Series schist. *Journal of Metamorphic Geology*, 26, 717-739.

Jessup, M.J., D.L. Newell, D.L, and J.M. Cottle (2008) Orogen-parallel extension and exhumation enhanced by denudation in the trans-Himalayan Arun River gorge, Ama Drime Massif, Tibet-Nepal. Geology: 36(7), 587–590.

Kaneko, Y., I. Katayama, H. Yamamoto, K. Misawa, M. Ishikawa, H. U. Rehman, A. B. Kausar, and K. Shiraishi (2003), Timing of Himalayan ultrahigh-pressure metamorphism: sinking rate and subduction angle of the Indian continental crust beneath Asia, J. Metamorph. Geol., 21(6), 589-599.

Kohn, M. J., E. J. Catlos, F. J. Ryerson, and T. M. Harrison (2002), Pressure-temperature-time path discontinuity in the Main Central thrust zone, Central Nepal: Reply, Geology, 30(5), 480-481.

Kretz, R. (1983), Symbols for rock-forming minerals, Am. Mineral., 68(1-2), 277-279.

Krogh, T. E. (1973), Low-Contamination Method for Hydrothermal Decomposition of Zircon and Extraction of U and Pb for Isotopic Age Determinations, Geochim. Cosmochim. Acta, 37(3), 485-494.

Law, R. D., M. P. Searle, and R. L. Simpson (2004), Strain, deformation temperatures and vorticity of flow at the top of the Greater Himalayan Slab, Everest Massif, Tibet, Journal of the Geological Society, 161, 305-320.

Le Roux, L. J. and L. E. Glendenin (1963), Half-life of ^{232}Th, Proceedings of the National Meeting on Nuclear Energy, Pretoria, South Africa, 83-94.

Leech, M. L., S. Singh, A. K. Jain, S. L. Klemperer, and R. M. Manickavasagam (2005), The onset of India-Asia continental collision: Early, steep subduction required by the timing of UHP metamorphism in the western Himalaya, Earth Planet. Sci. Lett., 234(1-2), 83-97.

Liu, Y., W. Siebel, H. Massonne, and X. Xiao (2007), Geochronological and petrological constraints for tectonic evolution of the central Greater Himalayan sequence in the Kharta area, southern Tibet., The Journal of Geology, 115, 215-242.

Lombardo, B., P. Pertusati, F. Rolfo, and D. Visoná (1998), First report of eclogites from the E Himalaya; implications for the Himalayan Orogeny, Memorie di Scienze Geologiche, 50, 67-68.

Lombardo, B. and F. Rolfo (2000), Two contrasting eclogite types in the Himalayas; implications for the Himalayan Orogeny, Journal of Geodynamics, 30(1-2), 37-60.

Ludwig, K. R. (1993), PBDAT: a computer program for processing Pb-U-Th isotope data, version 1.2, 88-542, 1-30.

Ludwig, K. R. (2003), Isoplot 3.00 A Geochronological Toolkit for Microsoft Excel, vol. 4, 71 pp., Berkeley Geochronology Center, Berkeley, California.

Martin, A. J., P. G. DeCelles, G. E. Gehrels, P. J. Patchett, and C. Isachsen (2005), Isotopic and structural constraints on the location of the Main Central thrust in the Annapurna Range, central Nepal Himalaya, Geological Society of America Bulletin, 117(7-8), 926-944.

Mattinson, J. M. (2005), Zircon U-Pb chemical abrasion ("CA-TIMS") method: Combined annealing and multi-step partial dissolution analysis for improved precision and accuracy of zircon ages, Chem. Geol., 220(1-2), 47-66.

Mezger, K., G. N. Hanson, and S. R. Bohlen (1989), High-Precision U-Pb Ages of Metamorphic Rutile - Application to the Cooling History of High-Grade Terranes, Earth Planet. Sci. Lett., 96(1-2), 106-118.

Miller, C., U. Klotzli, W. Frank, M. Thoni, and B. Grasemann (2000), Proterozoic crustal evolution in the NW Himalaya (India) as recorded by circa 1.80 Ga mafic and 1.84 Ga granitic magmatism, Precambrian Res., 103(3-4), 191-206.

Mukherjee, B. K. and H. K. Sachan (2001), Discovery of coesite from Indian Himalaya: a record of ultra-high pressure metamorphism in Indian continental crust., Current Science, 81, 1358-1361.

Mukherjee, B. K., H. K. Sachan, Y. Ogasawara, A. Muko, and N. Yoshioka (2003), Carbonate-bearing UHPM rocks from the Tso-Morari region, Ladakh, India: Petrological implications, Int. Geol. Rev., 45(1), 49-69.

Murphy, M. A. and T. M. Harrison (1999), Relationship between leucogranites and the Qomolangma Detachment in the Rongbuk Valley, South Tibet, Geology (Boulder), 27(9), 831-834.

Myrow, P. M., N. C. Hughes, T. S. Paulsen, I. S. Willlams, S. K. Parcha, K. R. Thompson, S. A. Bowring, S. C. Peng, and A. D. Ahluwalia (2003), Integrated tectonostratigraphic analysis of the Himalaya and implications for its tectonic reconstruction, Earth Planet. Sci. Lett., 212(3-4), 433-441.

Noble, S. R., J. Schwieters, D. J. Condon, Q. C. Crowley, N. Quaas, and R. R. Parrish (2006), TIMS characterization of new generation secondary electron multiplier, AGU Fall Meeting Abstracts.

O'Brien, P. J., N. Zotov, R. Law, M. A. Khan, and M. Q. Jan (2001), Coesite in Himalayan eclogite and implications for models of India-Asia collision, Geology, 29(5), 435-438.

Paquette, J. L., A. Nedelec, B. Moine, and M. Rakotondrazafy (1994), U-Pb, Single Zircon Pb-Evaporation, and Sm-Nd Isotopic Study of a Granulite Domain in Se Madagascar, J. Geol., 102(5), 523-538.

Parrish, R. R. (1987), An Improved Micro-Capsule for Zircon Dissolution in U-Pb Geochronology, Chem. Geol., 66(1-2), 99-102.

Parrish, R. R. (1990), U-Pb Dating of Monazite and its Application to Geological Problems, Canadian Journal of Earth Sciences, 27(11), 1431-1450.

Parrish, R. R. and K. V. Hodges (1996), Isotopic constraints on the age and provenance of the Lesser and Greater Himalayan sequences, Nepalese Himalaya, Geological Society of America Bulletin, 108(7), 904-911.

Parrish, R. R., S. J. Gough, M. P. Searle, and D. J. Waters (2006), Plate velocity exhumation of ultrahigh-pressure eclogites in the Pakistan Himalaya, Geology, 34(11), 989-992.

Pognante, U. and P. Benna (1993), Metamorphic zonation, migmatization and leucogranites along the Everest transect of eastern Nepal and Tibet; record of an exhumation history, Geological Society Special Publications, 74, 323-340.

Pognante, U. and D. A. Spencer (1991), 1st Report of Eclogites from the Himalayan Belt, Kaghan Valley (Northern Pakistan), European Journal of Mineralogy, 3(3), 613-618.

Powell, R., 1985, Regression Diagnostics and Robust Regression in Geothermometer Geobarometer Calibration - the Garnet Clinopyroxene Geothermometer Revisited: Journal of Metamorphic Geology, v. 3, p. 231-243.

Powell, R., and Holland, T.J.B., 1988, An internally consistent dataset with uncertainties and correlations; 3, Applications to geobarometry, worked examples and a computer program: Journal of Metamorphic Geology, v. 6, p. 173-204.

Richards, A., R. R. Parrish, N. B. W. Harris, T. Argles, and L. Zhang (2006), Correlation of lithotectonic units across the eastern Himalaya, Bhutan, Geology (Boulder), 34(5), 341-344.

Robinson, D. M., P. G. DeCelles, P. J. Patchett, and C. N. Garzione (2001), The kinematic evolution of the Nepalese Himalaya interpreted from Nd isotopes, Earth Planet. Sci. Lett., 192(4), 507-521.

Rolfo, F., W. McClelland, and B. Lombardo (2005), Geochronological Constraints on the Age of the Eclogite-facies Metamorphism in the Eastern Himalaya, Géologie Alpine, Mémoire H.S, 20th Himalaya-Karakorum-Tibet Workshop, Abstract Volume, 44, 170.

Schärer, U. (1984), The Effect of Initial Th-230 Disequilibrium on Young U-Pb Ages - the Makalu Case, Himalaya, Earth Planet. Sci. Lett., 67(2), 191-204.

Schelling, D. (1992), The Tectonostratigraphy and Structure of the Eastern Nepal Himalaya, Tectonics, 11(5), 925-943.

Searle, M. P. (1999), Extensional and compressional faults in the Everest-Lhotse massif, Khumbu Himalaya, Nepal, Journal of the Geological Society, 156, 227-240.

Searle, M. P., D. J. Waters, and B. J. Stephenson (2002), Pressure-temperature-time path discontinuity in the Main Central thrust zone, Central Nepal: Comment, Geology, 30(5), 479-480.

Searle, M. P., R. L. Simpson, R. D. Law, R. R. Parrish, and D. J. Waters (2003), The structural geometry, metamorphic and magmatic evolution of the Everest massif, High Himalaya of Nepal-South Tibet, Journal of the Geological Society, 160, 345-366.

Simonetti, A., L. M. Heaman, R. P. Hartlaub, R. A. Creaser, T. G. MacHattie, and C. Bohm (2005), U-Pb zircon dating by laser ablation-MC-ICP-MS using a new multiple ion counting Faraday collector array, J. Anal. At. Spectrom., 20(8), 677-686.

Simpson, R. L., R. R. Parrish, M. P. Searle, and D. J. Waters (2000), Two episodes of monazite crystallization during metamorphism and crustal melting in the Everest region of the Nepalese Himalaya, Geology, 28(5), 403-406.

Spencer, D. A., J. G. Ramsay, C. Spencer-Cervato, U. Pognante, M. N. Chaudhry, and M. Ghazanfar (1990), High pressure (eclogite facies) metamorphism in the Indian Plate, NW Himalaya, Pakistan, Geological Bulletin, University of Peshawar, 23, 87-100.

Stacey, J. S. and J. D. Kramers (1975), Approximation of Terrestrial Lead Isotope Evolution by a 2-Stage Model, Earth Planet. Sci. Lett., 26(2), 207-221.

Tera, F. and G. J. Wasserburg (1972), U-Th-Pb Systematics in Lunar Highland Samples from Luna-20 and Apollo-16 Missions, Earth Planet. Sci. Lett., 17(1), 36-51.

Tonarini, S., I. M. Villa, F. Oberli, M. Meier, D. A. Spencer, U. Pognante, and J. G. Ramsay (1993), Eocene Age of Eclogite Metamorphism in Pakistan Himalaya - Implications for India Eurasia Collision, Terra Nova, 5(1), 13-20.

Vannay, J. and K. V. Hodges (1996), Tectonometamorphic evolution of the Himalayan metamorphic core between the Annapurna and Dhaulagiri, central Nepal, J. Metamorph. Geol., 14(5), 635-656.

Veevers, J. J. (2007), Pan-Gondwanaland post-collisional extension marked by 650-500 Ma alkaline rocks and carbonatites and related detrital zircons: A review, Earth-Sci. Rev., 83(1-2), 1-47.

Viskupic, K. and K. V. Hodges (2001), Monazite-xenotime thermochronometry: methodology and an example from the Nepalese Himalaya, Contributions to Mineralogy and Petrology, 141(2), 233-247.

Viskupic, K., K. V. Hodges, and S. A. Bowring (2005), Timescales of melt generation and the thermal evolution of the Himalayan metamorphic core, Everest region, eastern Nepal, Contributions to Mineralogy and Petrology, 149(1), 1-21.

Wendt, I. and C. Carl (1991), The statistical distribution of the mean squared weighted deviation, Chemical Geology; Isotope Geoscience Section, 86(4), 275-285.

Wiedenbeck, M., P. Alle, F. Corfu, W. L. Griffin, M. Meier, F. Oberli, A. Vonquadt, J. C. Roddick, and W. Speigel (1995), 3 Natural Zircon Standards for U-Th-Pb, Lu-Hf, Trace-Element and REE Analyses, Geostandards Newsletter, 19(1), 1-23.

Zhang, J. and G. Lei (2007), Structure and geochronology of the southern Xainza-Dinggye rift and its relationship to the south Tibetan detachment system, Journal of Asian Earth Sciences, 29(5-6), 722-736.

Appendix 1 – U(-Th)-Pb Geochronology analytical techniques

ID-TIMS

Bulk separates of zircon from AD43 were annealed in high-purity quartz crucibles in air at 850°C for 48 hours, following the chemical abrasion method of *Mattinson*, [2005]. They were subsequently leached in Teflon® capsules for 12hrs at 180ºC in 29M HF + trace HNO_3. Prior to dissolution, selected zircon, titanite and rutile crystals were washed in distilled 2N HNO_3 at ~60 °C, followed by ultra-pure water. Zircon dissolution was performed with 29M HF and trace 2N HNO_3 for 3 days at 240ºC in Parrish-type PFA Teflon microcapsules [*Parrish*, 1987], dried down and converted to chloride form with 3.1 M HCl at 140ºC for 12 hours prior to chemistry. Titanite and rutile were also dissolved in 29M HF-trace HNO_3 over 5 days at 180ºC in modified Krogh type PTFE Teflon capsules [*Corfu and Noble,* 1992]. Prior to chemistry all fractions were spiked using a mixed ^{205}Pb-^{230}Th-^{233}U-^{235}U tracer. U and Pb chemical separations for zircon followed [*Krogh*, 1973] with modifications [*Corfu and Noble,* 1992]. Titanite and rutile U separation methods are modified from *Davis et al. [*1997] while and Pb separations followed the method of *Corfu and Grunsky,* [1987]. Data were obtained on a ThermoElectron Triton mass spectrometer fitted with a modified Mascom high linearity ion-counting secondary electron multiplier (SEM) following the analytical procedures of *Noble et al. [*2006]. A solution made from the zircon standard 91500 was measured along with several U and Pb blanks which averaged <0.1pg and <10pg respectively. All data were therefore reduced assuming a maximum of 10 pg procedural blank, the remainder being allocated to common Pb intrinsic to the mineral. The common Pb isotope composition was estimated for zircon using the two-stage model of [*Stacey and Kramers,* 1975].

LA-MC-ICPMS

Two laser ablation Multi Collector Inductively Coupled Plasma Mass Spectrometers (LA-MC-ICPMS) (a VG Elemental Axiom and a Nu Instruments Nu Plasma HR) both at the NIGL were used to obtain U(-Th)-Pb ages on monazite and U-Pb ages on zircon, xenotime, uranothorite and thorium oxide. Analytical protocols are modified from *Horstwood et al. [*2003] by the addition of a Th-Pb acquisition sequence on the Axiom.

U-Pb analyses on the Nu Plasma reflect the approach of *Horstwood et al. [*2003] modified for the collector arrangement of this instrument as detailed by Simonetti et al. [2005] with the addition of a collector to simultaneously monitor Hg to allow an on-line common-Pb correction. Monazite and zircon unknowns were normalized against matrix-matched primary reference materials (the 554Ma Manangotry monazite [*Paquette et al.,* 1994] and the 1065Ma 91500 zircon [*Wiedenbeck et al.,* 1995] respectively). Unfortunately, at the time of analysis well-characterized xenotime and uranothorite standards were not available, therefore xenotime analyses were normalized to Manangotry monazite while uranothorites were normalized to a combination of 91500 zircon (U-Pb) and Manangotry monazite (Th-Pb) to match ablation conditions and Th contents as closely as possible.

In-situ analyses were performed on separated grains mounted in 25mm epoxy resin discs and in polished thin sections (AD36). Backscatter electron (BSE) images were acquired for all crystals using a scanning electron microscope (SEM) (Fig. 6, 7). Grains that displayed complex BSE patterns were further imaged for Y, Th, U and Ce using an Electron Microprobe (EMP) in order to gain information on the internal compositional zonation and growth history. BSE, Y, Th and U images were also used to select spot locations for analysis such that multiple domains were avoided where possible (Fig. 10-13). Monazite, xenotime and zircon were analyzed using static spots of 35µm, 50µm and 25µm in diameter respectively.

Figure Captions

Figure 1. Simplified geological map of the central Himalayan orogen (modified from *Searle et al.* [2003]. The black box represents the area covered by the detailed map in Fig. 2. Inset: digital elevation model (USGS GTOPO 30) of the India Asia collision zone.

Figure 2. Digital elevation model (using Shuttle Radar Topography Mission (SRTM) 90 data) with geological summary map of the Ama Drime - Mt. Everest Region compiled from field observations and those of *Burchfiel et al.* [1992] as well as interpolation of ETM 7+ Landsat images (boxed area in Fig. 1). The white box represents the location of photograph in Fig. 3a. The geographic locations of samples and figures referred to in the text are arrowed.

Figure 3. Photographs of outcrops of granulitized mafic eclogite bodies within the ADM. A) Photograph B) and interpretation of the outcrop (N28° 07.878' E87° 17.477'; elevation: 4285 m.a.sl) within the core of the Ama Drime Massif. Locations of leucogranite sample AD35 and Ama Drime orthogneiss gneiss AD36 analyzed for U(-Th)-Pb geochronology are shown. A small sample of granulitized mafic eclogite was also recovered from the core of the mafic lens. The white box represents the location of photograph in Fig. 4a. Photograph looking north. Note Geologist (bottom center) for scale. C-E) Field photographs of granulitized mafic eclogites within the Ama Drime Massif. The geographic locations of all photographs are shown on Fig 2. C) Mafic lens offset by steeply west-dipping melt-filled fault with apparent top-down-to the west displacement. E) Localized parasitic folding of mafic layers and foliation in the host orthogneiss west of the main ADM fold axis. Note Geologists for scale in (C) and (E) while the mafic lense in (E) is approximately 40 – 60cm thick.

Figure 4. Outcrop photographs of orthogneisses in the Kharta region. The geographic location of these photographs is shown on Fig. 2 and 3a. A) Early Proterozoic (~ 1.8 Ga) Ama Drime orthogneiss showing top-down to the west and top-down to the east conjugate sets of melt filled extensional shear bands (arrowed), areas with deformed

augen of K-feldspar (lower right) and the presence of dark-colored foliation parallel lenses of Grt-Bt amphibolite (lower-right). Samples AD36 (orthogneiss) and AD35 (leucogranite) were collected approximately 1 and 3 meters respectively below the field of view. B) Ordovician-age (~470 Ma) orthogneiss from the hanging wall ~700m structurally above the Ama Drime detachment (ADD). The photograph is taken perpendicular to the foliation. Note the well-developed S-C fabric, indicating top-down to the west, normal sense of shear and deformed leucosomes (arrowed). Sample AD41 was collected at a similar structural level approximately one kilometer along strike from the location this photograph.

Figure 5. Backscattered electron (BSE) Scanning Electron Microscope (SEM) images of textures within AD43, mafic granulitized eclogite. A) Garnet and associated Pl + Hbl + Opx ± Bt corona. Note inclusions of Rt + Qtz +Zrn within garnet and replacement of rutile by titanite in the core of the garnet. B) Typical matrix with intergrown amphibole (Hbl) + biotite (Bt). C) Detailed view of Pl + Cpx ± Hbl ± Opx symplecite after omphacite. D)Inclusions of Rt + Qtz + Zrn within garnet and minor replacement of rutile by titanite.

Figure 6. Note All scale bars are 50 µm. A-B) X-ray chemical maps of U concentration of selected monazites from AD35 (orthogneiss) (A) and AD36 (leucogranite) (B). Brighter domains correspond to higher elemental concentrations. Crystals show simple two-domain zoning, with a low U core recording monazite growth during crystallization of the protolith granite at ~1.8 Ga and a high U rim formed at ~ 11 – 13 Ma (See Fig. 7 for details). The dark patches on the crystals are the locations of 35µm diameter LA-MC-ICPMS spot analyses. The apparent $^{208}Pb/^{232}Th$ age ± error (2σ absolute) is given for the analysis. Refer to Table 2 for the full analytical data set. C-L) Backscattered electron (BSE) scanning electron microscope images of selected zircon (C-F, I-L), monazite (G-H) and uranothorite (K-L) analyzed in this study. The lighter colored areas are enriched in Th and U relative to the darker areas, although note that due to manipulation grey-scale intensities are not necessarily directly comparable between images.

C-F) Zircons from sample AD36, Ama Drime orthogneiss. C) and D) are oscillatory-zoned euhedral crystals with the former containing a well-developed rim that poikiloblastically encloses quartz, feldspar, U-Th silicates and oxides and apatite. E) and F) are squat zircon prisms. E) Contains two large cavities (the largest black regions in the centre of the crystal) as well as abundant inclusions of quartz, feldspar, U-Th silicate and oxide (e.g. bright inclusions in the centre of F) and apatite.

G) textural setting and detailed view (H) of monazite 009 from the Ama Drime orthogneiss (AD36). The monazite is enclosed within the foliation-forming (S_a) sillimanite (Sil), and its age therefore constrains the maximum timing of high-temperature in-situ melting to 13.2 ± 1.4 Ma (see text for further details). The dashed circle is the location of a 35μm diameter LA-MC-ICPMS spot analysis. The $^{208}Pb/^{232}Th$ age ± error (2σ absolute) is given for the analysis. Refer to Table 2 for the full analytical data set. All scale bars are 50μm.

I) and J) are typical oscillatory-zoned zircon crystals analyzed from AD41, a migmatitic orthogneiss from the hanging wall of the ADD. K) and L) are uranothorites, also from AD41, darker regions represent metamict areas that are associated with radiogenic lead loss. The dashed boxes in D, I and J are the locations of 35 μm square LA-MC-ICPMS area rasters while the dashed circles in F and H and K are 20 μm diameter spot analyses. In D, F, I, J, K the $^{206}Pb/^{238}U$ age ± error (2σ absolute) for each analysis is quoted. Refer to Tables 3 and 4 for the full analytical data set.

Figure 7. U(-Th)-Pb concordia plots (error ellipses are 2σ) for monazite, zircon, xenotime, uranothorite and thorium oxide for samples dated by LA-MC-ICPMS and discussed in the text. See Tables 2-4 for full data set. All plots with the exception of (D and E) are common-lead corrected. A) All monazite data for leucogranite AD3 B) Six youngest monazite analyses from AD35 plotted on a Pb-Th concordia diagram. C) All monazite, xenotime and zircon data from orthogneiss AD36. D) Youngest monazite analyses from AD36 plotted on a Pb-Th concordia diagram. E) Un-corrected U-Pb concordia plot for all zircon and uranothorite analyses from AD41. Box indicates area covered in Fig. 7f. F) Un-corrected U-Pb concordia plot for all uranothorite data. The

dashed ellipse is excluded from the final age determination; the thick error ellipse represents the calculated concordia age, see text for further details.

Figure 8. A-D) Plane polarized light photographs of rutile (A), and zircon (B-D) from AD43 (a granulitized eclogite from ADM) and analyzed by ID-TIMS. Two distinct populations of zircon occur in AD43, the first and dominant sub-population consist of pinkish acicular crystals (B-C) that occasionally contain melt(?) inclusions (C) and clear, gem-quality squat prisms up to 40µm in diameter (D). E) Representative Cathodoluminescence (CL) images of zircon from AD43. Note the presence in some grains of thin highly luminescent rims, the presence of oscillatory and/or patchy zoning. Note that due to manipulation grey-scale intensities are not necessarily directly comparable between images. All scale bars are 50µm.

Figure 9. Secondary electron scanning electron microscope (SEM) images of zircons analyzed by LA-MC-ICPMS. Zircon grains were mounted on tape and analyzed using line rasters (A-B) and spots (C) to evaluate the presence of a rim domain(s). Line rasters (arrowed in A and B) had x:y:z dimensions of 100µm x 15µm x 2µm, while spots were 20µm in diameter and ~16µm deep. All scale bars are 50µm.

Figure 10. U-Pb concordia plots for zircon from AD43 analyzed by LA-MC-ICPMS. A) Line rasters and B) spot analyses. These analyses indicate that there is no resolvable difference in age between grain surfaces and cores.

Figure 11. U-Pb concordia (A) Common-lead (B) and Tera Wasserburg concordia (C) plots for zircon titanite and rutile analysed by ID-TIMS from sample AD43.

Table 1. Representative SEM-EDS mineral analyses for AD43.

Table 2. U-Th-Pb isotope data for monazites analysed by Axiom LA-MC-ICPMS.

Table 3. U-Pb isotope data for xenotime, thorium oxide and zircon analyzed by Axiom LA-MC-ICPMS.

Table 4. U-Pb isotope data for zircon and uranothorite analyzed by Nu Plasma LA-MC-ICPMS.

Table 5. U-Pb data ID-TIMS isotope data for zircon titanite and rutile from sample AD43.

Table 6. Representative SEM-EDS analyses and Y_{mnz} temperatures for monazite rims from AD36.

Table 1. Representative SEM-EDS mineral analyses for AD43.

AD43 mafic granulitized eclogite	Garnet			Clinopyroxene			Orthopyroxene		Plagioclase				Biotite				Amphibole		
Textural setting[1]	Core	Mantle	Rim	Symplectite	Grt Corona	incl. in Grt	Symplectite	Grt Corona	Symplectite	Grt Corona	Matrix	incl. in Grt	Symplectite	Grt Corona	Matrix	incl. in Grt	Symplectite	Grt Corona	Matrix
no. of analyses[2]	20	14	9	12	10	8	13	10	12	11	8	4	3	8	10	3	6	8	10
SiO_2	37.65	38.05	37.68	52.65	52.14	52.92	50.34	51.06	56.97	52.75	56.84	55.57	37.08	36.15	36.36	37.32	44.26	44.27	42.64
TiO_2	0.04	0.12	0.03	0.23	0.08	0.25	0.08	0.07	-	-	-	-	5.27	5.12	5.23	5.81	1.83	1.82	1.43
Al_2O_3	21.44	21.83	21.66	1.13	0.74	0.86	0.44	0.59	27.35	30.16	27.56	28.52	14.02	14.60	14.78	14.63	11.03	10.94	12.72
FeO	24.09	24.71	25.23	10.58	10.42	10.87	30.57	29.84	0.17	0.23	0.15	0.22	17.24	18.48	18.71	18.20	15.70	15.64	16.26
MnO	0.52	0.47	0.65	0.16	0.08	0.17	0.41	0.38	-	-	-	-	0.05	0.02	0.03	0.04	0.08	0.07	0.09
MgO	3.40	4.78	3.99	12.93	12.90	12.98	16.09	16.98	-	-	-	-	12.47	11.58	11.85	11.85	10.96	10.99	10.42
CaO	12.62	10.24	10.55	22.47	22.01	22.60	0.66	0.56	8.91	11.97	8.99	10.32	0.07	0.08	0.03	0.07	11.60	11.57	10.88
Na_2O	-	-	-	0.28	0.25	0.26	-	-	6.33	4.52	6.25	5.05	0.15	0.30	0.26	0.23	1.41	1.41	1.56
K_2O	-	-	-	-	-	-	-	-	0.26	0.12	0.25	0.18	10.47	10.37	10.34	10.26	1.16	1.15	1.26
TOTAL	99.76	100.19	99.78	100.44	98.62	100.93	98.58	99.48	99.99	99.75	100.04	99.86	96.83	96.70	97.60	98.41	98.02	97.85	97.27
no of oxygen atoms	24	24	24	6	6	6	6	6	8	8	8	8	22	22	22	22	23	23	23
Si	5.93	5.93	5.93	1.97	1.98	1.97	1.99	1.99	2.56	2.39	2.55	2.50	5.56	5.46	5.44	5.51	6.53	6.54	6.31
Ti	0.00	0.01	0.00	-	-	0.01	-	-	-	-	-	-	0.59	0.58	0.59	0.64	0.20	0.20	0.16
Al	3.98	4.01	4.01	0.05	0.03	0.04	0.02	0.03	1.45	1.61	1.46	1.51	2.48	-	2.61	2.55	1.92	1.90	2.22
Fe	3.17	3.22	3.32	0.33	0.33	0.34	1.01	0.97	0.01	0.01	0.01	0.01	2.16	2.34	2.34	2.25	1.94	1.93	2.01
Mn	0.07	0.06	0.09	-	-	0.01	0.01	0.01	-	-	-	-	0.01	-	-	-	0.01	0.01	0.01
Mg	0.80	1.11	0.94	0.72	0.73	0.72	0.95	0.99	-	-	-	-	2.79	2.61	2.64	2.61	2.41	2.42	2.30
Ca	2.13	1.71	1.78	0.90	0.90	0.90	0.03	0.02	0.43	0.58	0.43	0.50	0.01	0.01	0.01	0.01	1.83	1.83	1.72
Na	-	-	-	0.02	0.02	0.02	-	-	0.55	0.40	0.54	0.44	0.04	0.09	0.08	0.07	0.40	0.40	0.45
K	-	-	-	-	-	-	-	-	0.01	0.01	0.01	0.01	2.00	2.00	1.97	1.93	0.22	0.22	0.24
TOTAL	2.93	16.05	16.06	3.99	4.00	4.00	4.01	4.01	5.00	5.00	5.00	4.97	15.64	13.09	15.69	15.57	15.45	15.45	15.41

[1] textural classification of mineral analyses (See text for further detail)
[2] Number of analyses averaged

Table 2. U-Th-Pb isotope data for monazites analysed by Axiom LA-MC-ICPMS.

			Uncorrected Isotopic Ratios								Uncorrected Ages						Common-Pb Corrected Isotopic Ratios[d]									Common-Pb corrected Ages					
Name	Th (ppm)[a]	Th/U[b]	$^{207}Pb/^{206}Pb$	2σ%	$^{206}Pb/^{238}U$	2σ%	$^{207}Pb/^{235}U$	2σ%	$^{208}Pb/^{232}Th$	2σ%	$^{206}Pb/^{238}U$	2σ (Ma)	$^{207}Pb/^{235}U$	2σ (Ma)	$^{208}Pb/^{232}Th$	2σ (Ma)	f206%[c]	$^{207}Pb/^{206}Pb$	2σ%	$^{206}Pb/^{238}U$	2σ%	$^{207}Pb/^{235}U$	2σ%	$^{208}Pb/^{232}Th$	2σ%	$^{206}Pb/^{238}U$	2σ (Ma)	$^{207}Pb/^{235}U$	2σ (Ma)	$^{208}Pb/^{232}Th$	2σ (Ma)
Sample AD35 (Leucogranite) monazite																															
025-1	32185	6.0	0.1121	16.7	0.0018	1.92	0.0277	16.83	0.00058	3.55	11.56	0.22	27.77	4.73	11.71	0.42	1.0	0.0573	122.0	0.0016	9.02	0.0127	122.30	0.00053	8.405	10.4	0.9	12.8	15.7	10.8	0.9
030-1	31738	2.4	0.0405	15.2	0.0019	1.88	0.0106	15.32	0.00053	3.33	12.25	0.23	10.73	1.65	10.79	0.36	2.4	0.0455	55.0	0.0019	4.23	0.0121	55.21	0.00053	7.585	12.4	0.5	12.2	6.8	10.7	0.8
025-2	36532	5.5	0.0775	16.1	0.0020	1.75	0.0209	16.24	0.00058	3.30	12.56	0.22	20.96	3.44	11.68	0.39	1.3	0.0613	74.3	0.0020	6.30	0.0167	74.57	0.00055	7.379	12.7	0.8	16.8	12.6	11.2	0.8
023-1	28889	2.2	0.0459	12.4	0.0020	2.37	0.0129	12.58	0.00056	3.29	13.09	0.31	12.99	1.64	11.27	0.37	2.6	0.0615	42.1	0.0021	3.92	0.0181	42.26	0.00062	7.298	13.7	0.5	18.2	7.7	12.5	0.9
023-2	29684	2.3	0.0548	14.4	0.0021	1.79	0.0155	14.48	0.00058	3.41	13.23	0.24	15.64	2.28	11.70	0.40	2.3	0.0565	49.6	0.0021	4.32	0.0162	49.82	0.00059	8.054	13.4	0.6	16.4	8.2	11.9	1.0
033-1	31804	5.2	0.0580	27.9	0.0022	2.25	0.0173	27.96	0.00110	6.30	13.92	0.31	17.41	4.90	22.28	1.40	1.1	0.0264	285.2	0.0021	8.00	0.0076	285.30	0.00105	7.208	13.5	1.1	7.7	22.0	21.3	1.5
004-1	23000	2.8	0.0631	14.3	0.0022	2.10	0.0192	14.42	0.00082	4.62	14.24	0.30	19.36	2.82	16.60	0.77	1.7	0.0644	43.0	0.0022	4.37	0.0200	43.18	0.00084	7.788	14.5	0.6	20.1	8.7	17.0	1.3
001-1	26864	2.8	0.1068	8.0	0.0029	13.06	0.0420	15.33	0.00689	10.38	18.37	2.40	41.81	6.53	138.70	14.44	6.0	0.0823	12.9	0.0026	15.26	0.0300	20.01	0.00678	10.4853	17.0	2.6	30.1	6.1	136.5	14.4
028-2	32551	2.9	0.0870	8.0	0.0040	1.93	0.0482	8.18	0.00540	4.32	25.85	0.50	47.79	4.00	108.95	4.72	3.6	0.0601	30.4	0.0039	3.11	0.0326	30.52	0.00528	4.316	25.3	0.8	32.6	10.1	106.5	4.6
028-1	31733	3.0	0.0777	9.9	0.0044	2.24	0.0474	10.11	0.00235	20.01	28.45	0.64	47.00	4.86	47.47	9.51	2.9	0.0390	54.8	0.0043	2.85	0.0231	54.88	0.00226	20.504	27.6	0.8	23.2	12.8	45.7	9.4
010-1	23820	9.3	0.1037	7.6	0.0130	3.51	0.1854	8.34	0.01608	5.21	83.06	2.94	172.74	15.65	322.40	16.93	5.0	0.1125	11.3	0.0136	3.85	0.2110	11.95	0.01624	5.219	87.1	3.4	194.4	25.4	325.6	17.1
012-1	11540	2.4	0.0998	7.3	0.0142	4.25	0.1953	8.42	0.01612	5.45	90.89	3.89	181.15	16.62	323.29	17.77	6.7	0.1008	10.8	0.0144	4.08	0.2000	11.51	0.01611	5.341	92.1	3.8	185.1	23.2	323.0	17.4
017-1	30579	4.2	0.1089	7.1	0.0615	3.67	0.9234	7.98	0.03171	3.61	384.56	14.54	664.13	73.49	630.96	23.13	43.3	0.1093	2.2	0.0625	3.65	0.9421	4.24	0.03174	3.527	391.0	14.7	674.0	40.2	631.7	22.6
008-1	26961	7.3	0.1092	7.1	0.0698	3.47	1.0506	7.90	0.04145	4.36	434.98	15.59	729.19	82.62	820.84	36.49	20.5	0.1093	3.4	0.0729	3.87	1.0979	5.13	0.04148	4.304	453.5	18.1	752.4	56.4	821.5	36.1
018-1	26282	4.1	0.1098	7.1	0.0943	2.34	1.4278	7.46	0.05502	3.33	580.87	14.23	900.62	105.39	1082.64	36.99	64.8	0.1114	1.6	0.0960	2.34	1.4741	2.82	0.05515	3.250	591.0	14.5	919.8	41.8	1085.1	36.2
015-1	31147	11.5	0.1103	7.1	0.1942	2.29	2.9539	7.45	0.06118	3.45	1144.16	28.61	1395.86	211.95	1200.19	42.65	42.3	0.1096	2.1	0.1975	2.33	2.9846	3.15	0.06139	3.384	1162.0	29.6	1403.7	93.3	1204.2	41.9
014-1	32419	9.1	0.1107	7.1	0.2575	1.67	3.9310	7.28	0.06617	3.60	1476.78	27.69	1620.09	271.59	1295.09	48.07	76.5	0.1102	1.4	0.2617	1.70	3.9747	2.22	0.06620	3.516	1498.5	28.6	1629.0	87.8	1295.5	47.0
Sample AD36 (Ama Drime orthogneiss) monazite																															
010-1	15754	3.3	0.1	11.6	0.0020	2.44	0.0371	11.82	0.00062	5.71	12.74	0.62	36.99	8.90	12.58	1.44	1.0	0.1	46.6	0.0019	3.28	0.0287	23.55	0.00056	5.729	12.1	0.8	28.8	13.7	11.4	1.3
020-1	14484	3.6	0.1	7.7	0.0022	3.03	0.0435	10.20	0.00078	5.24	14.47	0.88	43.28	9.01	15.81	1.66	1.2	0.0	53.7	0.0018	3.55	0.0049	>50	0.00061	5.922	11.6	0.8	5.0	12.0	12.2	1.4
009-1	16839	4.6	0.2	1.6	0.0027	3.72	0.0609	8.57	0.00091	5.01	17.10	1.27	60.07	10.59	18.30	1.83	1.5	0.1	72.9	0.0021	4.80	0.0174	36.74	0.00065	5.452	13.5	1.3	17.5	13.0	13.2	1.4
026-1	11514	3.1	0.1	72.9	0.0020	2.55	0.0192	15.65	0.00066	4.45	12.94	0.66	19.29	6.09	13.41	1.20	1.3	0.1	87.8	0.0021	4.77	0.0198	44.14	0.00067	9.157	13.5	1.3	19.9	17.7	13.6	2.5
013-1	16205	5.4	0.1	15.4	0.0282	13.63	0.4241	13.72	0.02367	8.73	179.12	49.42	358.99	116.50	472.87	83.42	18.8	0.1	4.5	0.0286	6.90	0.4343	7.26	0.02369	4.348	181.6	25.4	366.2	63.1	473.3	41.6

[a]Th content in ppm accurate to approximately 10%.
[b]Normalised to Th/U ratio of the standard
[c]Percentage of ^{206}Pb that is common
[d]Isotopic ratios are corrected for common-Pb. Common-Pb correction based on a two-stage model (Stacey and Kramers, 1975) and the interpreted age of the crystal

Table 3. U-Pb isotope data for xenotime, thorium oxide and zircon analysed by Axiom LA-MC-ICPMS.

		Uncorrected Isotopic Ratios							Uncorrected Ages				Common-Pb Corrected Isotopic Ratios[d]								Common-Pb corrected Ages			
Name	U (ppm)[a]	$^{207}Pb/^{206}Pb$	2σ%	$^{206}Pb/^{238}U$	2σ%	$^{207}Pb/^{235}U$	2σ%	Rho[b]	$^{206}Pb/^{238}U$	2σ (Ma)	$^{207}Pb/^{235}U$	2σ (Ma)	f206%[c]	$^{207}Pb/^{206}Pb$	2σ%	$^{206}Pb/^{238}U$	2σ%	$^{207}Pb/^{235}U$	2σ%	Rho[b]	$^{206}Pb/^{238}U$ age	2σ (Ma)	$^{207}Pb/^{235}U$	2σ (Ma)
Sample AD36 Ama Drime orthogneiss - zircon																								
za008-1	54	0.0935	4.781	0.3082	4.780	3.9735	6.761	0.7	1732	94	1629	128	0.00	0.1186	16.985	0.3244	5.152	5.3031	17.749	0.3	1811	107	1869	674
za015-1	263	0.1102	2.036	0.2537	4.641	3.8544	5.068	0.9	1457	75	1604	95	0.00	0.1136	5.851	0.2524	4.580	3.9527	7.430	0.6	1451	74	1625	261
za019-1	64	0.0950	4.384	0.3003	4.892	3.9328	6.569	0.7	1693	94	1620	123	0.00	0.1044	19.118	0.3026	5.171	4.3566	19.805	0.3	1704	100	1704	632
za019-2	319	0.1114	2.296	0.1219	4.630	1.8724	5.168	0.9	741	36	1071	48	0.08	0.1087	9.324	0.1202	4.583	1.8015	10.389	0.4	732	35	1046	174
za021-1	31	0.1013	8.926	0.2949	4.566	4.1204	10.027	0.5	1666	86	1658	191	0.00	0.0992	39.619	0.2941	5.741	4.0219	40.032	0.1	1662	108	1639	974
za021-2	148	0.0839	3.499	0.2091	5.265	2.4186	6.322	0.8	1224	71	1248	75	0.00	0.1021	18.265	0.2158	5.812	3.0361	19.168	0.3	1259	80	1417	466
za021-3	134	0.1075	2.637	0.2787	4.514	4.1324	5.228	0.9	1585	81	1661	104	0.00	0.1084	10.251	0.2775	4.582	4.1486	11.228	0.4	1579	81	1664	388
Sample AD36 Ama Drime orthogneiss - xenotime																								
xn1	22606	0.0520	7.161	0.0020	1.495	0.0142	3.658	0.4	12.8	0.4	14.3	2.1	0.19	0.0515	12.395	0.0020	0.935	0.0141	12.430	0.1	12.8	3.6	14.2	0.2
xn2	4553	0.1106	5.316	0.3013	2.185	4.5966	5.748	0.4	1697.8	42.4	1748.7	252	0.13	0.1098	0.952	0.3013	2.230	4.5625	2.425	0.9	1698	109	1742	43
xn3	7664	0.0937	9.852	0.0021	1.841	0.0266	5.011	0.4	13.3	0.5	26.7	5.4	6.59	0.0463	43.590	0.0019	2.702	0.0120	43.674	0.1	12.1	10.6	12.1	0.7
Sample AD36 Ama Drime orthogneiss - U-Th oxide inclusions in zircon																								
Th 042	102961	0.0717	68.131	0.001	10.427	0.015	68.924	0.2	9.5	1.0	14.8	10.2	4.27	0.4634	52.008	0.0015	22.297	0.0988	56.586	0.4	10.0	2.2	95.7	55.2
Th 039	517275	0.0664	45.078	0.002	9.066	0.017	45.981	0.2	11.9	1.1	17.0	7.9	1.92	0.0585	24.562	0.0019	5.811	0.0150	25.240	0.2	12.0	0.7	15.1	3.8

[a]U content in ppm accurate to approximately 10%.
[b]Rho is the error correlation coefficient calculated following Ludwig [1993].
[c]Percentage of ^{206}Pb that is common
[d]Isotopic ratios are corrected for common-Pb. Common-Pb correction based on a single-stage model (Stacey and Kramers, 1975) and the interpreted age of the crystal

Table 4. U-Pb isotope data for zircon and uranothorite analysed by Nu Plasma LA-MC-ICPMS.

		Uncorrected Isotopic Ratios							Uncorrected Ages				
Name	U (ppm)[a]	$^{207}Pb/^{206}Pb$	2σ%	$^{206}Pb/^{238}U$	2σ%	$^{207}Pb/^{235}U$	2σ%	Rho[b]	$^{206}Pb/^{238}U$	2σ (Ma)	$^{207}Pb/^{235}U$	2σ (Ma)	f206%[c]
Sample AD41 Kharta orthogneiss - zircon													
z001-1	359	0.05687	0.646	0.06625	2.243	0.51951	2.334	1.0	413.5	9.6	424.8	12.2	0.07
z005-1	284	0.05621	0.356	0.07193	1.556	0.55749	1.596	1.0	447.8	7.2	449.9	9.0	0.04
z005-2	551	0.05543	0.301	0.07251	1.428	0.55417	1.459	1.0	451.3	6.7	447.7	8.2	0.06
z010-1	57	0.05620	0.820	0.07181	1.298	0.55650	1.536	0.8	447.1	6.0	449.2	8.6	0.04
z010-2	49	0.05647	0.683	0.07201	1.778	0.56065	1.904	0.9	448.3	8.2	452.0	10.8	0.09
z010-3	19	0.05550	1.818	0.07137	2.365	0.54611	2.983	0.8	444.4	10.9	442.4	16.4	0.07
z007-1	28	0.05729	1.212	0.07144	1.614	0.56428	2.018	0.8	444.8	7.4	454.3	11.5	0.06
z007-2	56	0.05659	0.714	0.06558	1.810	0.51172	1.946	0.9	409.5	7.6	419.6	10.1	0.02
z007-3	21	0.05727	1.694	0.06530	2.157	0.51562	2.743	0.8	407.8	9.1	422.2	14.3	0.01
z007-4	45	0.05546	1.144	0.06071	4.348	0.46426	4.496	1.0	379.9	17.0	387.2	21.0	0.02
z014-1	52	0.05642	1.684	0.06541	1.842	0.50886	2.496	0.7	408.5	7.8	417.7	12.8	0.05
z014-2	45	0.05841	1.056	0.06967	1.853	0.56106	2.133	0.9	434.1	8.3	452.2	12.1	0.04
z014-3	68	0.05615	0.787	0.07050	2.177	0.54582	2.315	0.9	439.1	9.9	442.3	12.7	0.02
Sample AD41 Kharta orthogneiss - uranothorite													
ut003-1	235854	0.04711	2.108	0.00246	1.996	0.01596	2.903	0.7	15.8	0.3	16.1	0.5	0.01
ut003-2	249826	0.04678	2.128	0.00236	2.794	0.01521	3.512	0.8	15.2	0.4	15.3	0.5	0.01
ut007-1	266749	0.04655	2.105	0.00242	3.738	0.01553	4.290	0.9	15.6	0.6	15.6	0.7	0.01
ut007-2	262293	0.04714	2.229	0.00244	2.787	0.01588	3.569	0.8	15.7	0.4	16.0	0.6	0.07
ut007-3	273316	0.04595	2.117	0.00244	3.171	0.01545	3.813	0.8	15.7	0.5	15.6	0.6	0.05
ut009-1	311575	0.04648	2.137	0.00241	2.666	0.01547	3.417	0.8	15.5	0.4	15.6	0.5	0.09
ut009-2	300578	0.04645	2.132	0.00251	3.018	0.01607	3.696	0.8	16.2	0.5	16.2	0.6	0.05
ut009-3	305213	0.04623	2.115	0.00248	2.896	0.01584	3.586	0.8	16.0	0.5	16.0	0.6	0.09
ut009-4	306382	0.04569	2.107	0.00248	2.605	0.01565	3.351	0.8	16.0	0.4	15.8	0.5	0.04
Sample AD43 Granulitized eclogite - zircon spot analyses													
018-1	498	0.07142	2.3	0.15394	3.0	1.51584	3.8	0.8	923	31	937	58	0.07
018-2	479	0.07333	2.3	0.15505	3.0	1.56764	3.8	0.8	929	31	957	59	0.04
018-3	565	0.07278	2.1	0.16190	3.3	1.62468	3.9	0.8	967	36	980	64	0.06
016-1	1019	0.07258	1.5	0.15302	3.4	1.53122	3.7	0.9	918	35	943	57	0.04
016-2	1379	0.07211	1.2	0.16158	3.0	1.60641	3.2	0.9	966	32	973	52	0.09
011-1	585	0.07167	2.2	0.14412	3.2	1.42408	3.8	0.8	868	30	899	55	0.07
011-2	688	0.07188	1.9	0.16112	3.0	1.59694	3.5	0.8	963	32	969	56	0.06
011-3	611	0.07196	2.0	0.15513	3.3	1.53921	3.9	0.9	930	34	946	60	0.02
025-1	256	0.07281	3.7	0.13428	4.6	1.34801	5.9	0.8	812	41	867	79	0.01
024-1	437	0.07095	2.6	0.14247	4.1	1.39367	4.9	0.8	859	39	886	68	0.02
014-1	413	0.07282	2.6	0.15555	2.9	1.56185	3.9	0.7	932	30	955	61	0.05
014-2	461	0.07220	2.5	0.15123	2.9	1.50549	3.8	0.8	908	29	933	57	0.04
014-3	416	0.07220	2.7	0.14299	2.9	1.42359	3.9	0.7	862	27	899	56	0.02
019-1	446	0.07275	2.4	0.16305	2.9	1.63552	3.8	0.8	974	32	984	62	0.01
019-2	453	0.07271	2.4	0.15664	2.8	1.57029	3.7	0.8	938	30	959	59	0.01
Sample AD43 Granulitized eclogite - zircon line raster analyses													
022-1	347	0.07171	3.2	0.14506	3.8	1.43435	5.0	0.8	873	36	903	71	0.07
022-2	395	0.07352	3.0	0.14653	4.1	1.48551	5.1	0.8	882	40	924	76	0.05
009-1	209	0.07746	7.4	0.11561	7.4	1.23473	10.4	0.7	705	56	816	127	0.09
018-1	266	0.07294	3.9	0.13648	5.7	1.37253	6.9	0.8	825	51	877	94	0.05
026-1	1233	0.07321	1.5	0.15802	4.0	1.59518	4.3	0.9	946	42	968	68	0.09
026-2	881	0.07297	1.7	0.15249	3.6	1.53421	4.0	0.9	915	36	944	61	0.04

[a]U content in ppm accurate to approximately 10%.
[b]Rho is the error correlation defined as err$^{206}Pb/^{238}U$ / err$^{207}Pb/^{235}U$
[c]Percentage of ^{206}Pb that is common

Table 5. U-Pb data ID-TIMS isotope data for zircon titanite and rutile from sample AD43.

	Concentrations [b]					Atomic ratios															Ages (Ma)			
Fractions [a]	Weight (mg)	U (ppm)	Pb (ppm)	Th/U	Common Pb (pg)	$^{206}Pb/^{204}Pb$ [c]	$^{207}Pb/^{206}Pb$ [d]	Error	$^{238}U/^{204}Pb$ [d]	Error	$^{204}Pb/^{206}Pb$ [d]	Error	$^{208}Pb/^{206}Pb$ [e]	$^{238}U/^{206}Pb$ [e]	Error	$^{207}Pb/^{235}U$ [e]	Error	$^{207}Pb/^{206}Pb$ [e]	Error	$^{206}Pb/^{238}U$	$^{207}Pb/^{235}U$	$^{207}Pb/^{206}Pb$	rho [f]
1. zr 3:1, eu, pk, 85µm, (1)	0.03	16.6	3.5	1.06	6.7	782.1	0.0902463	0.07	4662.28294	0.45	0.0012785	0.41	0.3255	6.09363	0.18	1.628848	0.24	0.0719872	0.14	979.55	981.41	985.58	0.80
2. zr 4:1, eu, pk, 90µm, (1)	0.03	37.3	7.8	1.05	14.7	719.4	0.0917681	0.08	4324.92537	0.51	0.0013900	0.48	0.3243	6.15756	0.17	1.610322	0.25	0.0719151	0.17	970.11	974.23	983.52	0.74
3. zr 4:1, eu, pk, 95µm, (1)	0.04	4.3	0.8	0.90	2.9	567.0	0.0970579	0.13	3459.18527	0.56	0.0017630	0.53	0.2838	6.28768	0.19	1.576138	0.33	0.0718759	0.27	951.45	960.85	982.42	0.61
4. zr 3:1, eu, pk, 80µm, (1)	0.03	35.4	6.9	1.10	1.6	5456.9	0.0742402	0.07	34292.50153	0.71	0.0001831	0.69	0.3456	6.30002	0.17	1.567527	0.19	0.0716235	0.07	949.71	957.45	975.28	0.92
5. zr 3:1, eu, pk, 120µm, (1)	0.02	14.6	2.4	0.63	3.9	589.8	0.0954386	0.12	4102.20368	0.58	0.0016951	0.51	0.2230	7.16097	0.29	1.371032	0.38	0.0712063	0.25	842.66	876.61	963.33	0.77
6. zr 4:1, eu, pk, 110µm, (1)	0.02	55.6	11.1	1.09	2.7	4849.0	0.0749173	0.09	29588.67386	0.79	0.0002062	0.77	0.3369	6.12133	0.21	1.621158	0.23	0.0719730	0.10	975.44	978.44	985.17	0.90
7. zr 1:1, eu, cl, 22µm (1)	0.01	4.9	0.8	0.15	3.0	178.8	0.1399403	0.29	1171.31536	2.75	0.0055920	2.74	0.0316	7.24097	0.36	1.120035	4.54	0.0588203	4.25	833.93	762.99	560.46	0.82
8. zr 1:1, eu, cl, 19µm, (1)	0.02	9.9	1.9	0.95	2.3	744.0	0.0903395	0.11	4745.62694	0.42	0.0013435	0.38	0.3056	6.52521	0.18	1.503059	0.26	0.0711327	0.18	919.17	931.63	961.23	0.72
9. zr 1:1, eu, cl, 25µm, (1)	0.02	4.9	0.7	0.09	1.4	549.1	0.0959643	0.12	3621.65859	0.44	0.0018200	0.39	0.0283	6.80258	0.20	1.416934	0.31	0.0699072	0.22	884.14	896.08	925.61	0.69
10. zr 1:1, eu, cl, 16µm, (1)	0.02	16.7	2.6	0.18	3.1	761.9	0.0890836	0.09	4954.23181	0.51	0.0013120	0.47	0.0567	6.64890	0.17	1.457996	0.25	0.0703081	0.17	903.21	913.18	937.38	0.73
11. zr 1:1, eu, cl, 13µm, (1)	0.02	4.1	0.5	0.09	2.2	308.4	0.1145192	0.12	2324.33499	0.50	0.0032415	0.47	0.0323	7.97552	0.19	1.175654	0.47	0.0680044	0.40	761.48	789.29	868.71	0.51
12. zr 1:1, eu, cl, 29µm, (1)	0.01	23.8	4.0	0.62	2.5	684.4	0.0908272	0.29	4590.17473	3.13	0.0014607	3.12	0.2014	6.87620	0.20	1.401905	1.12	0.0699143	1.03	875.29	889.74	925.84	0.52
13. rt 2:1, eu, 40µm, (35)	0.10	3.7	0.1	0.08	4	67.0	0.1925337	1.18	14012.89429	2.45	0.0080412	2.43	0.0445	112.6807	0.17	0.081809	14.5	0.0075574	0.47	1159.82	79.84	48.53	0.30
14. rt 1:1, eu, 38µm, (40)	0.10	3.3	0.1	2.44	5	29.5	0.4037031	0.93	8406.17112	1.60	0.0261542	1.58	-0.1688	219.8569	0.17	-0.003169	823.1	0.0023455	1.56	-5000.00	-3.22	15.10	0.15
15. rt 2:1, sub, 42µm, (45)	0.10	3.8	0.1	0.05	10	23.8	0.6419230	0.24	3018.68715	0.48	0.0397706	0.47	0.0295	120.0551	0.14	0.023400	336.6	0.0021563	1.63	1164.74	23.49	13.89	0.04
16. rt 3:1, an, 30µm, (45)	0.10	11.6	0.2	0.33	14	32.1	0.4896826	0.17	6167.30590	0.36	0.0290825	0.33	0.1743	179.3605	0.16	0.027040	168.1	0.0025596	0.58	1111.27	27.09	16.48	0.02
17. rt 3:1, eu, 51µm, (40)	0.10	9.9	0.5	0.11	21	105.0	0.2306476	0.20	3267.92544	0.28	0.0087790	0.27	0.0726	28.6890	0.10	0.449114	22.0	0.0291547	0.13	1827.65	376.66	185.26	0.02
18. rt 2:1, sub, 58µm, (30)	0.10	5.6	0.2	-0.11	18	23.0	0.6736036	0.35	2190.14018	0.45	0.0423945	0.41	-0.0415	92.8500	0.24	0.016417	1019.4	0.0022565	2.06	318.76	16.53	14.53	0.02
19. rt 1:1, sub, 29µm, (45)	0.10	7.0	0.2	0.22	15	27.2	0.5734345	0.41	3333.85247	0.54	0.0350451	0.49	0.1151	116.8353	0.28	0.030381	447.0	0.0029695	1.23	1046.97	30.39	19.11	0.02
20. rt 1:1, eu 32µm, (40)	0.10	5.1	0.1	0.2541	11.8	22.6	0.6795391	0.42	3372.25917	0.62	0.0426775	0.55	0.1094	143.9194	0.40	0.012042	1221.5	0.0014227	2.89	652.85	12.15	9.16	0.02
21. ttn 1:1, sub, 50µm, (25)	0.26	11.3	2.4	0.75	608.2	19.7	0.8024317	0.06	308.58100	0.24	0.0507277	0.12	0.8450	264.67709	1.94	0.087975	10.61	0.1688784	8.89	24.31	85.62	2546.56	0.91
22. ttn 1:1, sub, 55µm, (31)	0.36	4.6	2.3	0.05	804.9	19.8	0.8018788	0.05	130.61629	0.21	0.0505943	0.13	0.8056	107.25098	1.96	0.240335	9.53	0.1869460	7.77	59.83	218.69	2715.48	0.92
23. ttn 1:1, sub, 32µm, (25)	0.20	3.6	1.3	0.85	260.1	19.5	0.8100699	0.09	173.84998	1.04	0.0511887	0.13	1.1383	175.90276	2.62	0.161505	12.03	0.2060432	10.10	36.54	152.02	2874.68	0.78
24. ttn 1:1, sub, 35µm, (25)	0.24	5.4	1.3	0.73	305.0	19.7	0.8056341	0.07	268.07875	0.21	0.0507515	0.13	1.0543	231.77503	2.06	0.129906	9.22	0.2183708	7.52	27.75	124.01	2968.72	0.86

[a] zr = zircon, ttn = titantie, rt = rutile; l:w aspect ratio; eu = euhedral, sub = subhedral, an = anhedral; pk = pink, cl = colourless; length (µm); (x) = number of grains analysed.
[b] Maximum errors are ± 20%. Weights were calculated from grain dimensions measured on binocular microscope photos.
[c] Measured ratio corrected for mass fractionation and common Pb in the $^{205}Pb/^{235}U$ spike.
[d] Ratios corrected for spike, blank and fractionation only following Ludwig (1980)
[e] Corrected for mass fractionation, spike, laboratory blank Pb and U, and initial common Pb (Stacey and Kramers 1975; calculated at 1 Ga for zircon and 0.01 Ga for rutile and titanite, with an uncertainty of 2%).
The laboratory blank Pb composition is $^{206}Pb/^{204}Pb$:$^{207}Pb/^{204}Pb$:$^{208}Pb/^{204}Pb$ = 18.60 : 15.69 : 37.32. Quoted errors are 2 sigma (% for atomic ratios, absolute for ages).
[f] $^{207}Pb/^{235}U$ - $^{206}Pb/^{238}U$ error correlation coefficient calculated following Ludwig (1993).

Table 6. Representative SEM-EDS analyses and Y_{mnz} temperatures for monazite rims from AD36.

grain[a]	La_2O_3 [b]	Ce_2O_3 [b]	Pr_2O_3 [b]	Nd_2O_3 [b]	Sm_2O_3 [b]	Gd_2O_3 [b]	Y_2O_3 [b]	CaO [b]	ThO_2 [b]	UO_2 [b]	P_2O_5 [b]	Total	Y_{mnz} + HREE [c, d]	T°C at various P (kbar) 7	8	9	10	11	12	2σ absolute error (T°C) [e]
013 (4)	11.58	24.65	2.80	10.03	1.95	1.94	3.80	1.86	7.08	2.19	28.93	96.82	0.1267	800	782	765	748	732	717	58
009 (6)	12.25	25.29	2.97	9.98	2.08	1.74	3.51	1.61	5.99	2.56	28.85	96.82	0.1257	796	778	761	745	729	713	80
010 (5)	11.99	24.36	2.73	9.39	1.95	1.50	3.54	2.08	7.55	3.13	29.18	97.39	0.1167	762	744	727	710	695	679	50
020 (7)	11.61	24.43	2.79	10.18	1.99	1.60	3.80	1.84	7.23	2.53	29.07	97.06	0.1312	815	797	780	763	747	732	61
026 (7)	11.70	24.60	2.78	10.31	2.02	1.50	3.92	1.88	7.15	2.66	29.07	97.59	0.1289	807	789	772	756	740	724	71
031 (3)	11.66	24.55	3.12	10.31	1.95	1.75	3.77	1.79	6.69	2.73	29.35	97.68	0.1299	811	793	775	759	743	728	69

[a] Grain numbers refer to the same grains identified in Table 2. Value in parentheses refers to the number of analyses averaged.
[b] Measurements were made on the Scanning Electron Microscope (SEM) equipped with an Energy Dispersive System (EDS)
[c] Ymnz is the mole fraction of Y in monazite calculated assuming a total cationic occupancy of 1.
[d] HREE refers to the sum of the Heavy Rare Earth element (HREE) component (La - Lu inclusive) in the analyses
[e] Errors in T determined by propagating analytical uncertainties through all calculations

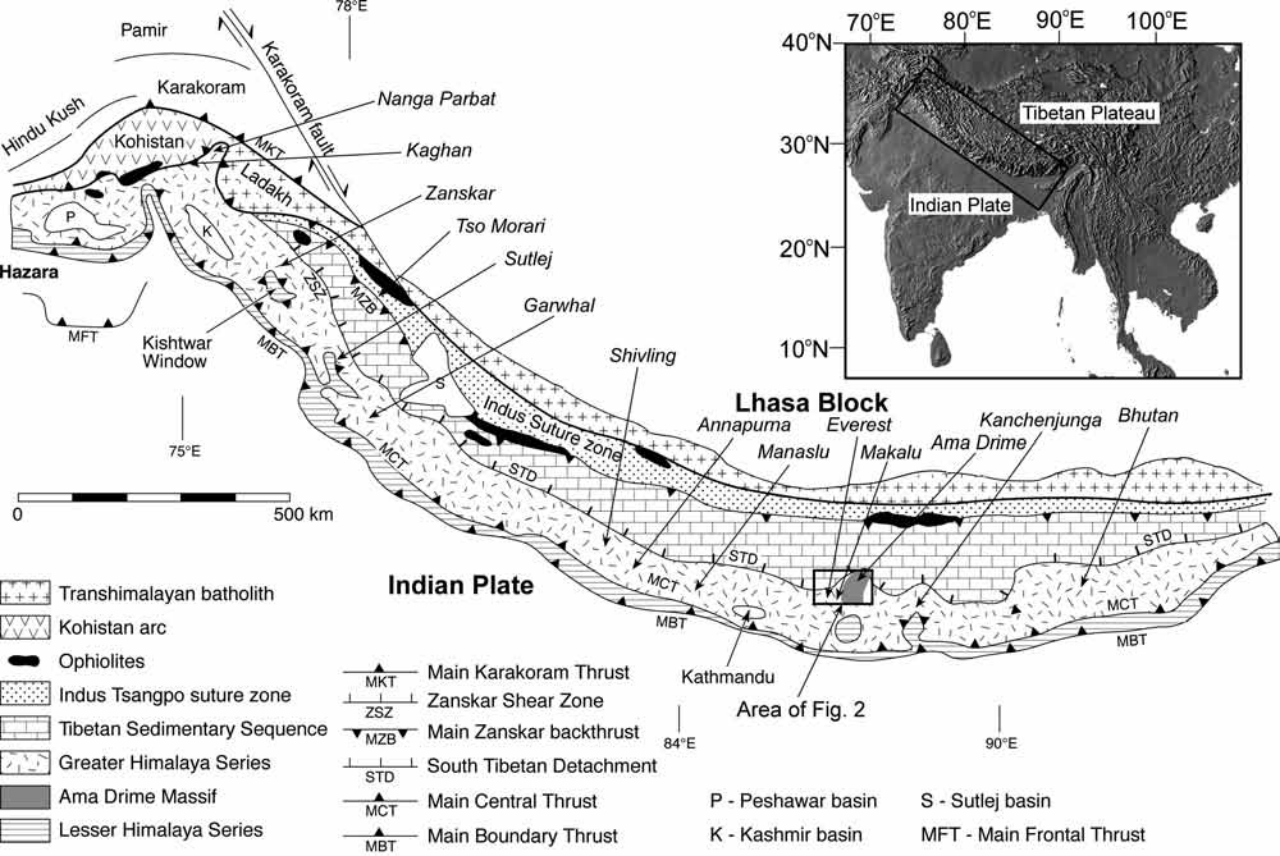
Pamir
78°E
Karakoram fault
Karakoram
Hindu Kush
Kohistan
MKT
Nanga Parbat
Kaghan
Ladakh
Zanskar
Tso Morari
Sutlej
Garwhal
Shivling
P
K
Hazara
MFT
Kishtwar Window
MBT
ZSZ
MZB
S
Indus Suture zone
MCT
STD
75°E
0
500 km
Lhasa Block
Annapuma
Everest
Kanchenjunga
Bhutan
Manaslu
Makalu
Ama Drime
Indian Plate
Kathmandu
Area of Fig. 2
84°E
90°E
70°E
80°E
90°E
100°E
40°N
30°N
20°N
10°N
Tibetan Plateau
Indian Plate
Transhimalayan batholith
Kohistan arc
Ophiolites
Indus Tsangpo suture zone
Tibetan Sedimentary Sequence
Greater Himalaya Series
Ama Drime Massif
Lesser Himalaya Series
MKT Main Karakoram Thrust
ZSZ Zanskar Shear Zone
MZB Main Zanskar backthrust
STD South Tibetan Detachment
MCT Main Central Thrust
MBT Main Boundary Thrust
P - Peshawar basin
K - Kashmir basin
S - Sutlej basin
MFT - Main Frontal Thrust

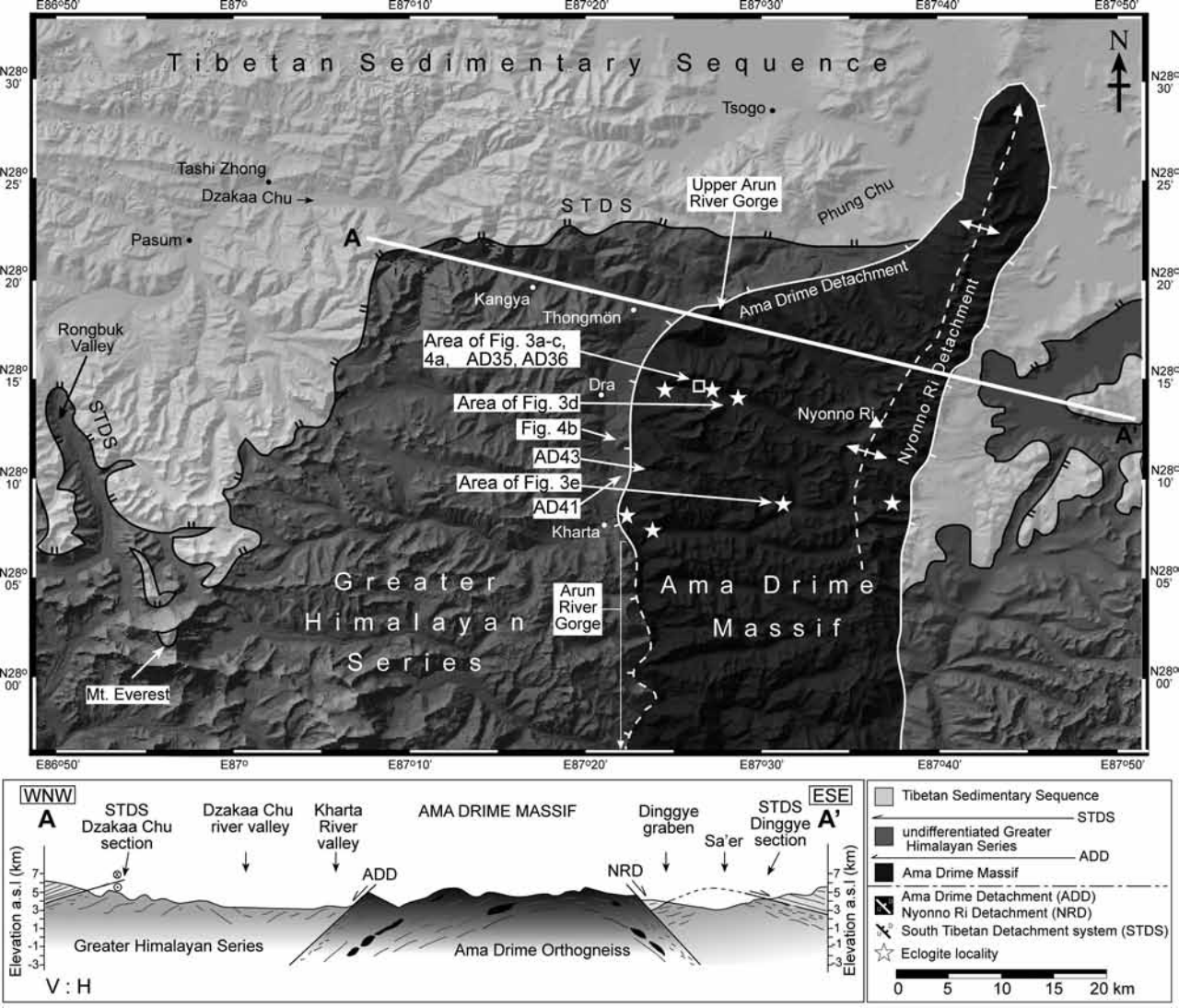
Tibetan Sedimentary Sequence
Tsogo
Tashi Zhong
Dzakaa Chu
Pasum
STDS
Upper Arun River Gorge
Phung Chu
A
Ama Drime Detachment
Kangya
Thongmön
Rongbuk Valley
STDS
Area of Fig. 3a-c, 4a, AD35, AD36
Dra
Area of Fig. 3d
Fig. 4b
AD43
Area of Fig. 3e
AD41
Kharta
Nyonno Ri
Nyonno Ri Detachment
A'
Greater Himalayan Series
Arun River Gorge
Ama Drime Massif
Mt. Everest
N
E86°50'
E87°
E87°10'
E87°20'
E87°30'
E87°40'
E87°50'
N28° 30'
N28° 25'
N28° 20'
N28° 15'
N28° 10'
N28° 05'
N28° 00'
WNW
A
STDS Dzakaa Chu section
Dzakaa Chu river valley
Kharta River valley
AMA DRIME MASSIF
Dinggye graben
Sa'er
STDS Dinggye section
ESE
A'
ADD
NRD
Elevation a.s.l (km)
Greater Himalayan Series
Ama Drime Orthogneiss
V : H
Tibetan Sedimentary Sequence
STDS
undifferentiated Greater Himalayan Series
ADD
Ama Drime Massif
Ama Drime Detachment (ADD)
Nyonno Ri Detachment (NRD)
South Tibetan Detachment system (STDS)
Eclogite locality
0 5 10 15 20 km

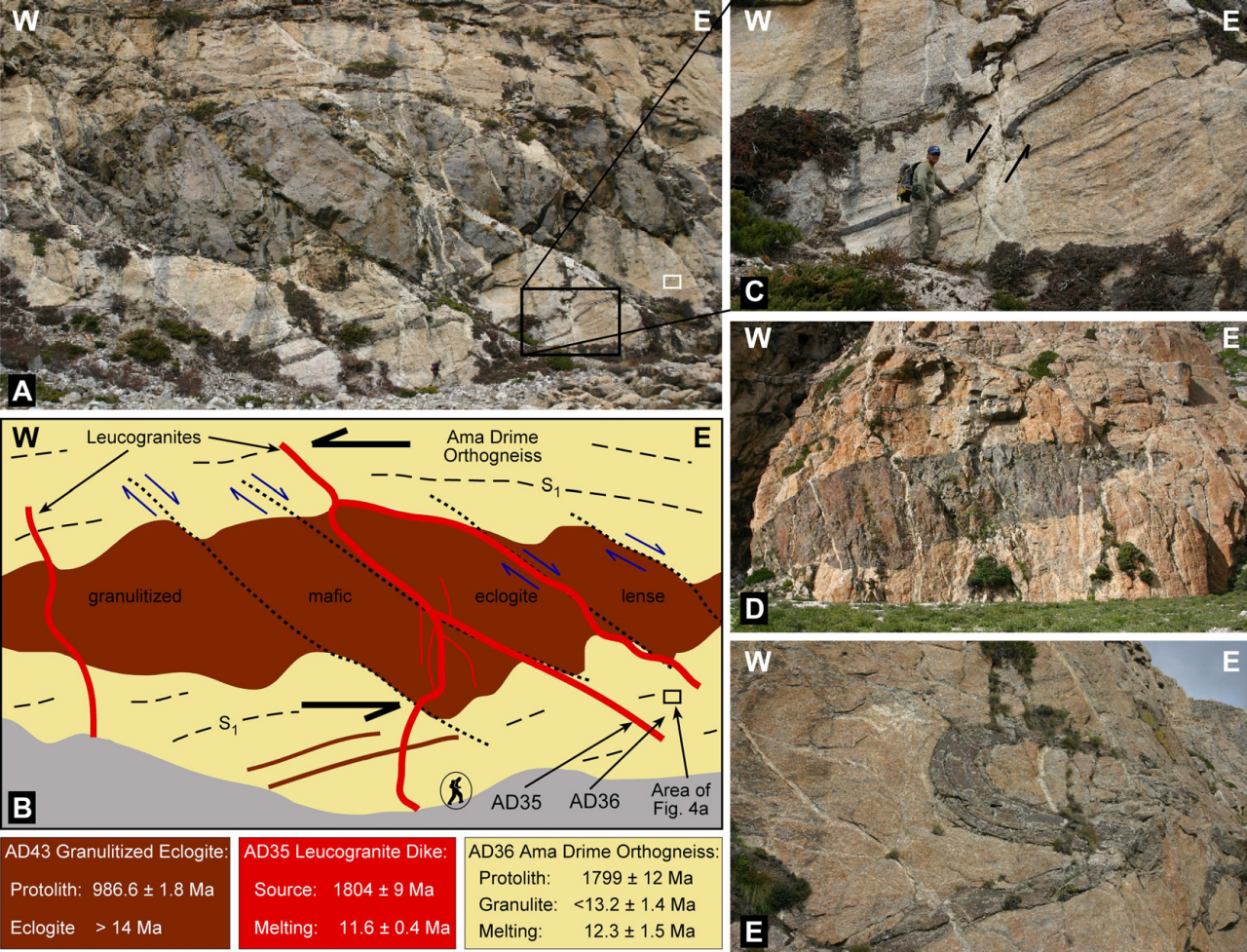

AD43 Granulitized Eclogite:	
Protolith:	986.6 ± 1.8 Ma
Eclogite	> 14 Ma

AD35 Leucogranite Dike:	
Source:	1804 ± 9 Ma
Melting:	11.6 ± 0.4 Ma

AD36 Ama Drime Orthogneiss:	
Protolith:	1799 ± 12 Ma
Granulite:	<13.2 ± 1.4 Ma
Melting:	12.3 ± 1.5 Ma


W
E
A

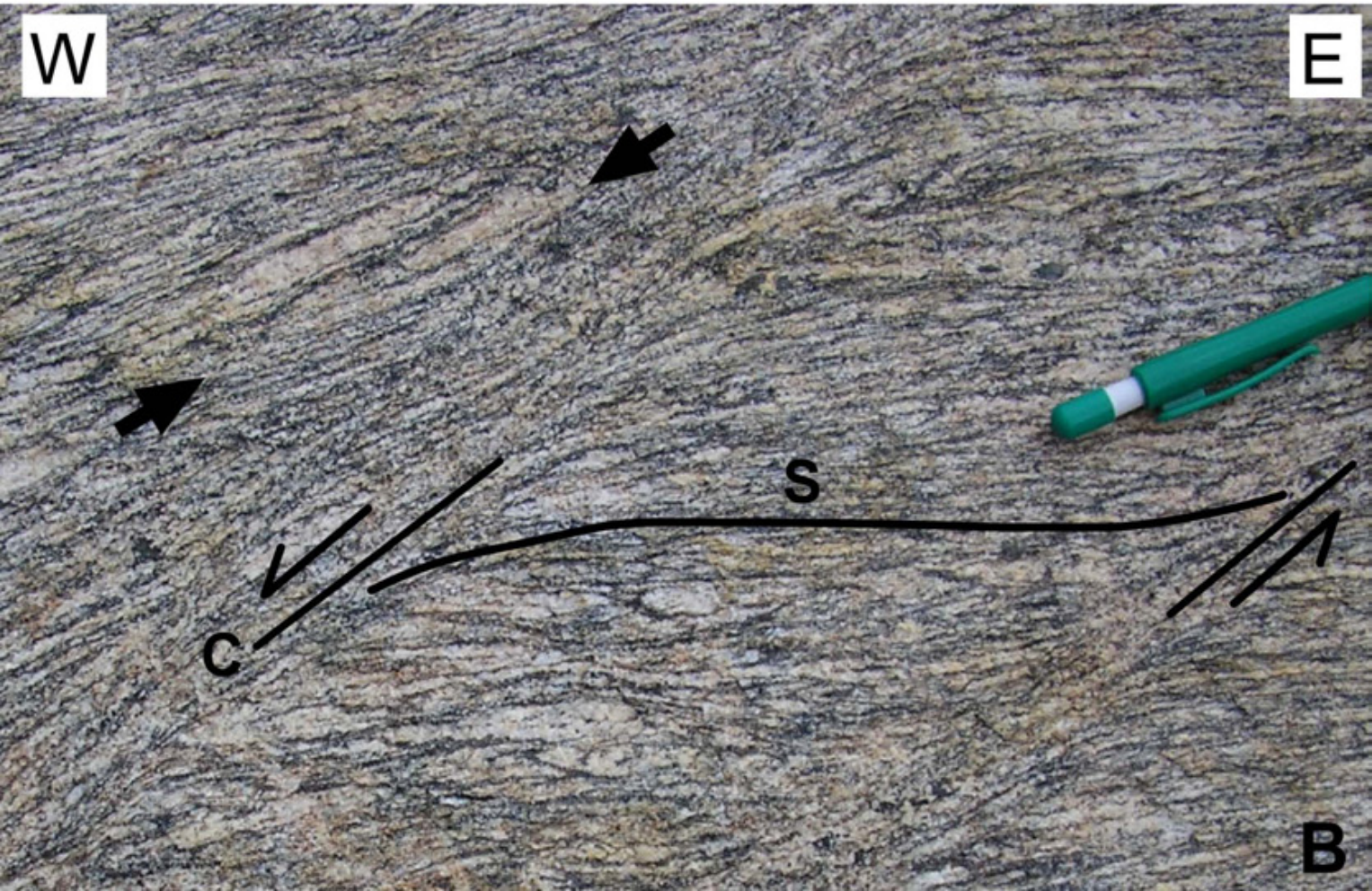
W
E
S
C
B

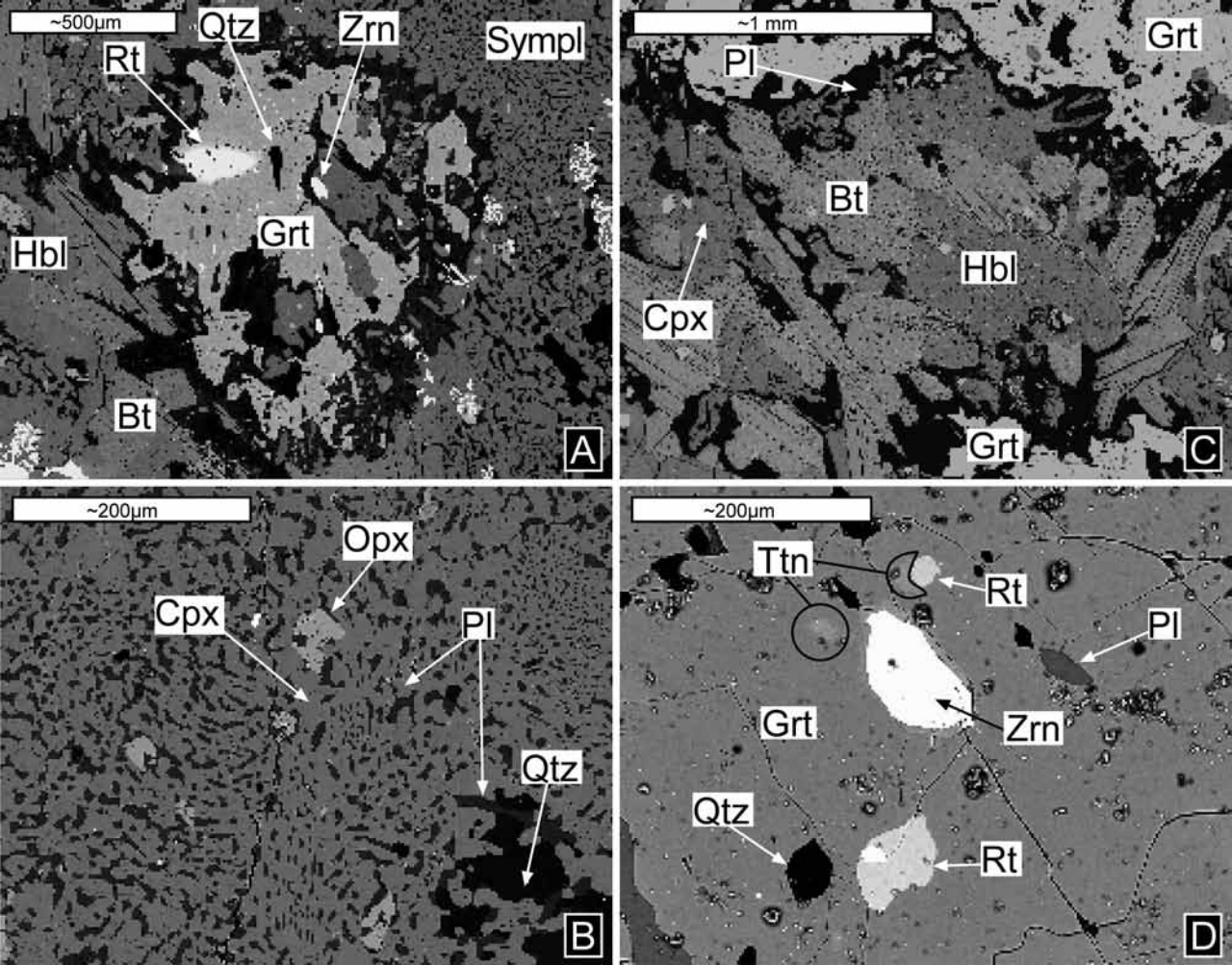
~500µm
Qtz
Zrn
Sympl
Rt
Grt
Hbl
Bt
A
~1 mm
Grt
Pl
Bt
Hbl
Cpx
Grt
C
~200µm
Opx
Cpx
Pl
Qtz
B
~200µm
Ttn
Rt
Pl
Grt
Zrn
Qtz
Rt
D

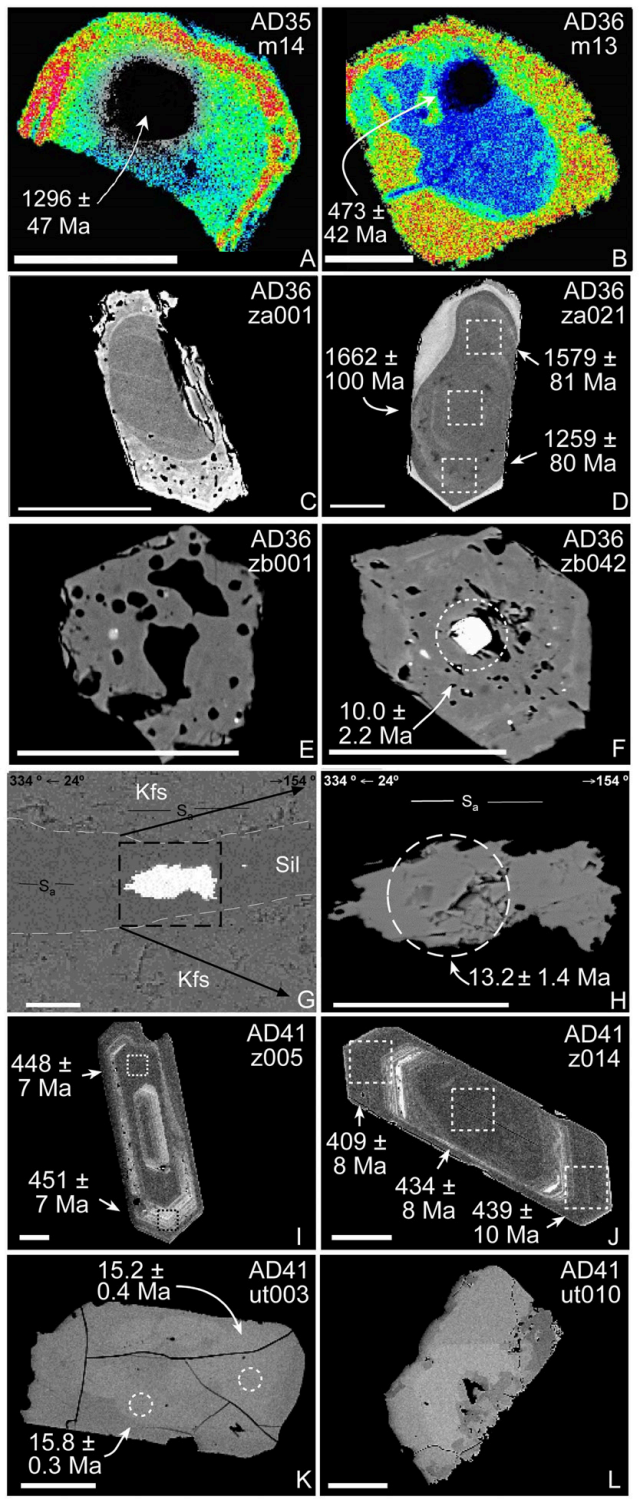
AD35
m14
1296 ±
47 Ma
A
AD36
m13
473 ±
42 Ma
B
AD36
za001
C
AD36
za021
1662 ±
100 Ma
1579 ±
81 Ma
1259 ±
80 Ma
D
AD36
zb001
E
AD36
zb042
10.0 ±
2.2 Ma
F
334 ° ← 24°
→154 °
Kfs
Sa
Sil
Sa
Kfs
G
334 ° ← 24°
→154 °
Sa
13.2 ± 1.4 Ma
H
AD41
z005
448 ±
7 Ma
451 ±
7 Ma
I
AD41
z014
409 ±
8 Ma
434 ±
8 Ma
439 ±
10 Ma
J
15.2 ±
0.4 Ma
AD41
ut003
15.8 ±
0.3 Ma
K
AD41
ut010
L

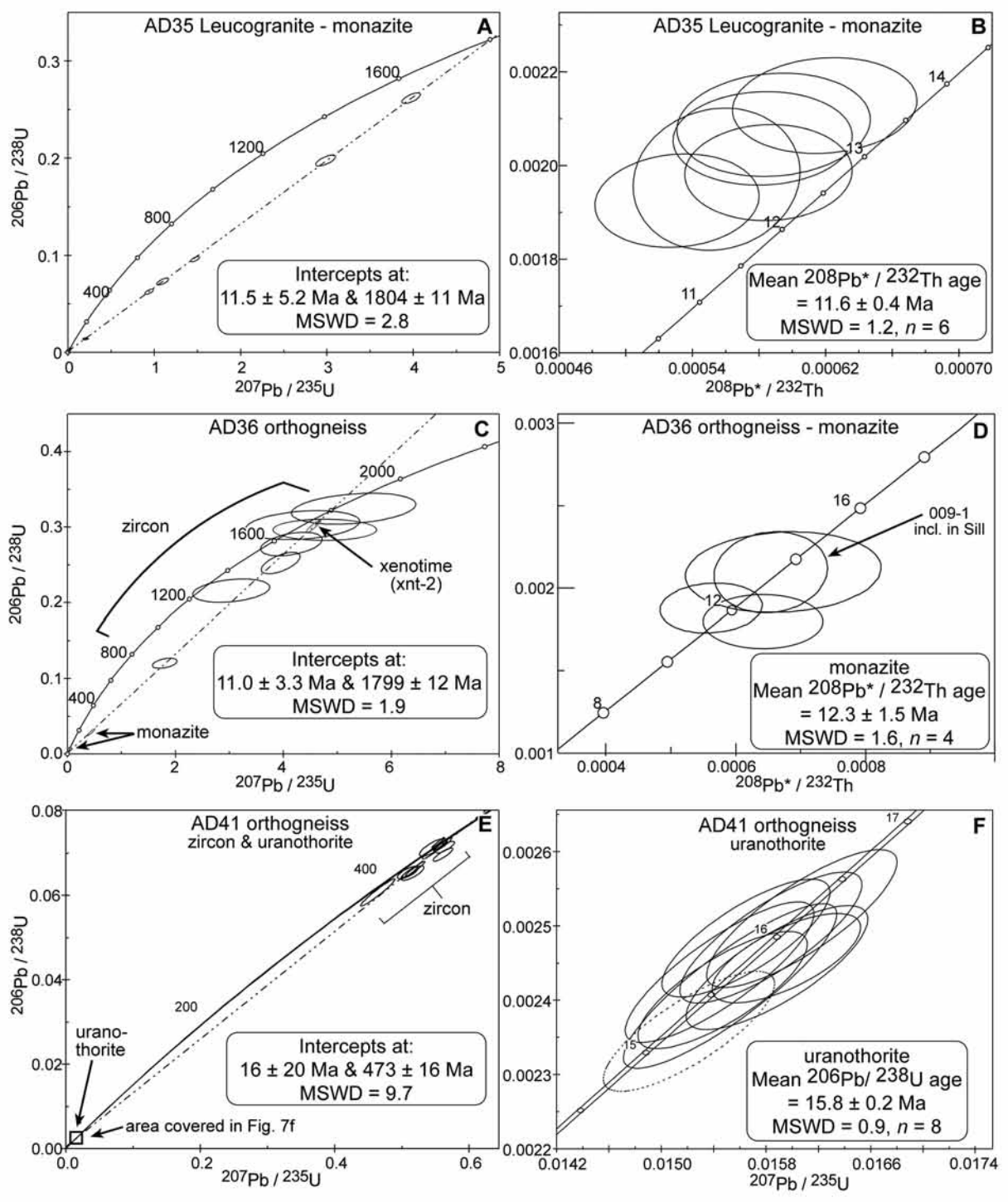
AD35 Leucogranite - monazite
A
Intercepts at:
11.5 ± 5.2 Ma & 1804 ± 11 Ma
MSWD = 2.8
206Pb / 238U
207Pb / 235U
AD35 Leucogranite - monazite
B
Mean 208Pb* / 232Th age
= 11.6 ± 0.4 Ma
MSWD = 1.2, n = 6
208Pb* / 232Th
AD36 orthogneiss
C
zircon
xenotime
(xnt-2)
monazite
Intercepts at:
11.0 ± 3.3 Ma & 1799 ± 12 Ma
MSWD = 1.9
AD36 orthogneiss - monazite
D
009-1
incl. in Sill
monazite
Mean 208Pb* / 232Th age
= 12.3 ± 1.5 Ma
MSWD = 1.6, n = 4
AD41 orthogneiss
zircon & uranothorite
E
zircon
urano-
thorite
area covered in Fig. 7f
Intercepts at:
16 ± 20 Ma & 473 ± 16 Ma
MSWD = 9.7
AD41 orthogneiss
uranothorite
F
uranothorite
Mean 206Pb/ 238U age
= 15.8 ± 0.2 Ma
MSWD = 0.9, n = 8

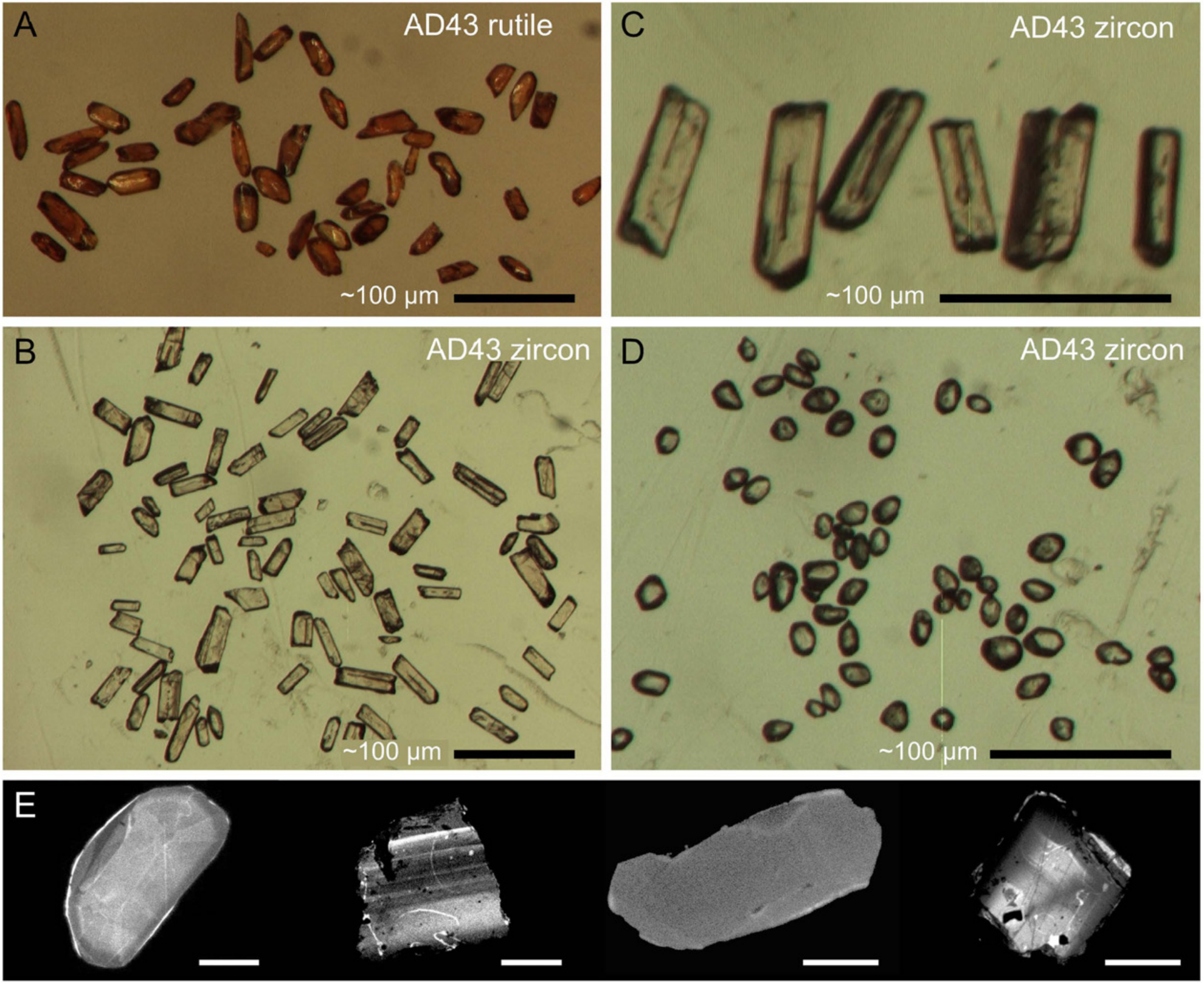
A
AD43 rutile
~100 µm
C
AD43 zircon
~100 µm
B
AD43 zircon
~100 µm
D
AD43 zircon
~100 µm
E

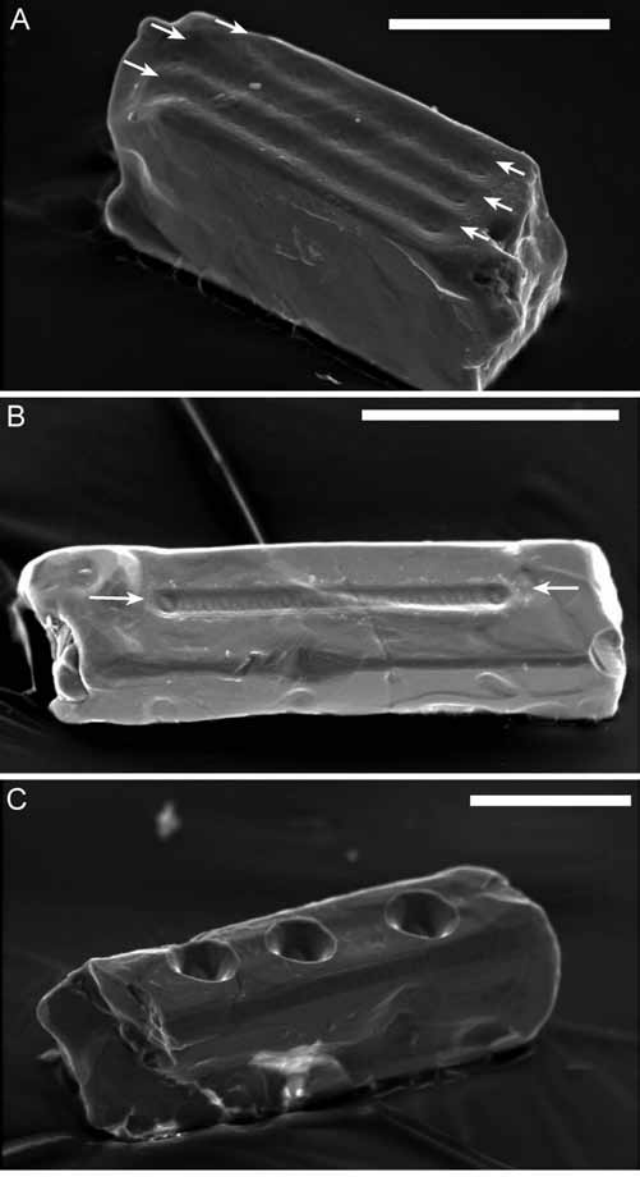
A
B
C

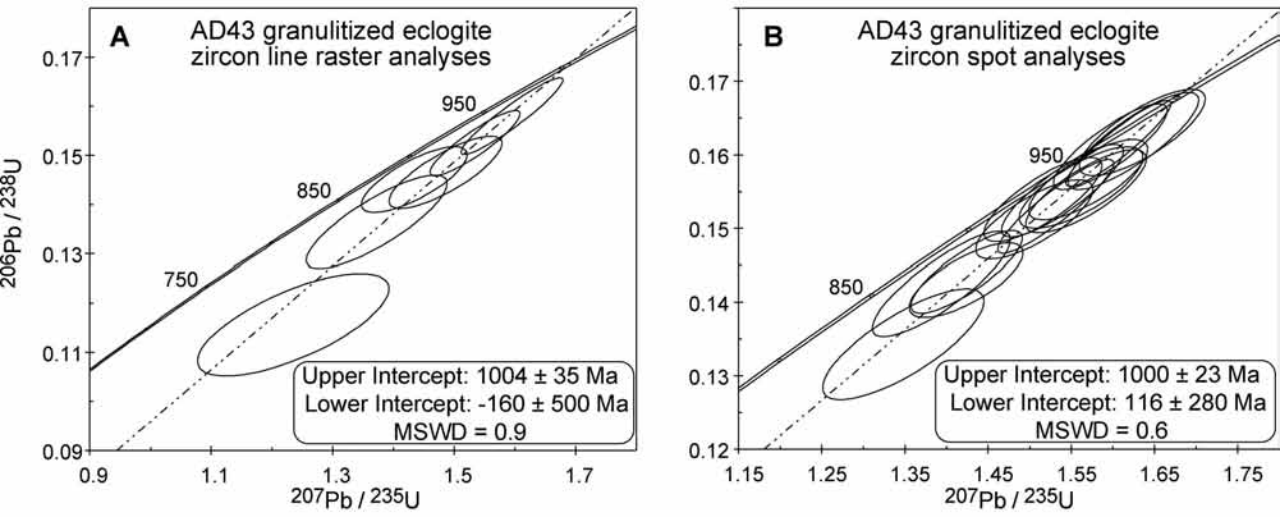
A
AD43 granulitized eclogite
zircon line raster analyses
950
850
750
Upper Intercept: 1004 ± 35 Ma
Lower Intercept: -160 ± 500 Ma
MSWD = 0.9
206Pb / 238U
207Pb / 235U
0.09
0.11
0.13
0.15
0.17
0.9
1.1
1.3
1.5
1.7
B
AD43 granulitized eclogite
zircon spot analyses
950
850
Upper Intercept: 1000 ± 23 Ma
Lower Intercept: 116 ± 280 Ma
MSWD = 0.6
207Pb / 235U
0.12
0.13
0.14
0.15
0.16
0.17
1.15
1.25
1.35
1.45
1.55
1.65
1.75

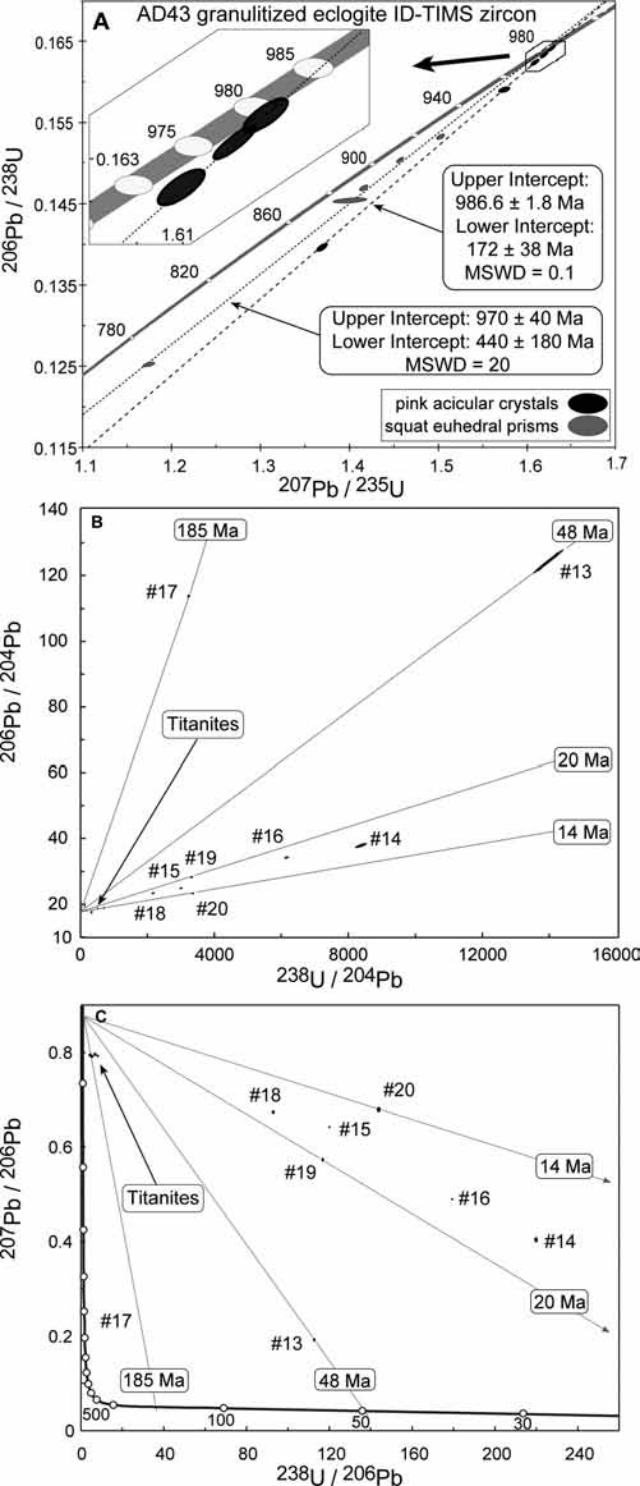
A
AD43 granulitized eclogite ID-TIMS zircon
Upper Intercept:
986.6 ± 1.8 Ma
Lower Intercept:
172 ± 38 Ma
MSWD = 0.1
Upper Intercept: 970 ± 40 Ma
Lower Intercept: 440 ± 180 Ma
MSWD = 20
pink acicular crystals
squat euhedral prisms
206Pb / 238U
207Pb / 235U
B
185 Ma
48 Ma
20 Ma
14 Ma
Titanites
#17
#13
#16
#14
#15
#19
#18
#20
206Pb / 204Pb
238U / 204Pb
C
Titanites
#18
#20
#15
#19
#16
#14
#17
#13
14 Ma
20 Ma
185 Ma
48 Ma
500
100
50
30
207Pb / 206Pb
238U / 206Pb